Disruption of desmoplastic stroma overcomes restrictions to T cell extravasation, immune exclusion and immunosuppression in solid tumors

Zebin Xiao[1], Zhen Lu[1], Leslie Todd[1], Li Huang[1], Meghan Kopp[1], Lili Huang[2], Wenqun Zhong[3], Yue Li[1], Wei Guo[3], John Scholler[4], Carl H. June[4], Steven M. Albelda[5] and Ellen Puré[1,6,*]

[1]Department of Biomedical Sciences, University of Pennsylvania, Philadelphia, PA 19104, USA

[2]Department of Pathology and Laboratory Medicine, Perelman School of Medicine, University of Pennsylvania, Philadelphia, PA 19104, USA

[3]Department of Biology, School of Arts & Sciences, University of Pennsylvania, Philadelphia, PA 19104, USA

[4]Center for Cellular Immunotherapies, Perelman School of Medicine, University of Pennsylvania, Philadelphia, PA 19104, USA

[5]Department of Medicine, Perelman School of Medicine, University of Pennsylvania, Philadelphia, PA 19104, USA

[6]Lead contact

***Corresponding author:** Ellen Puré, 380 S. University Avenue, Hill Pavilion 410E, Philadelphia, PA. 19104, USA; epure@upenn.edu

Abstract

The desmoplastic stroma in solid tumors presents a formidable challenge to immunotherapies that rely on endogenous or adoptively transferred T cells, however, the mechanisms are poorly understood. To define mechanisms involved, we treated established desmoplastic pancreatic tumors with CAR T cells directed to fibroblast activation protein (FAP), an enzyme highly overexpressed on a subset of cancer-associated fibroblasts (CAFs). Depletion of FAP^+CAFs resulted in loss of the structural integrity of desmoplastic matrix. This rendered these highly treatment-resistant cancers susceptible to subsequent treatment with a tumor antigen (mesothelin)-targeted CAR and to anti-PD1 antibody therapy. Mechanisms included overcoming stroma-dependent restriction of T cell extravasation and/or perivascular invasion, reversing immune exclusion, relieving T cell suppression, and altering the immune landscape by reducing myeloid cell accumulation and increasing endogenous $CD8^+$ T cell and NK cell infiltration. These data provide strong rationale for combining tumor stroma- and malignant cell-targeted therapies to be tested in clinical trials.

Keywords: tumor stroma, tumor microenvironment, FAP^+ cancer-associated fibroblasts, T cell tumor immunity

Main

Immunotherapies that rely on endogenous or adoptively transferred T cells have proven to be challenging in treating solid tumors[1-3]. To date, attempts to improve the efficacy of chimeric antigen receptor (CAR) T cells in solid tumors have focused on modifications to improve their intrinsic functionality, to increase their resistance to immunosuppressive factors, and enhance trafficking into tumors[4]. Unfortunately, attempts at translating these strategies to the clinic have also proved to be disappointing[5]. One reason for poor efficacy of tumor associated antigen (TAA)-targeted immunotherapies in solid tumors is the complex tumor microenvironment (TME) that insulates tumor cells against an effective cytotoxic immune responses[4]. Understanding and overcoming the barriers that exclude T cell infiltration and/or inhibit T cell function will be critical to achieving sustained efficacy of immunotherapies in most solid tumor patients.

Key components of the immunosuppressive TME in solid tumors are cancer-associated fibroblasts (CAFs) and the associated desmoplastic matrix[6, 7]. Previous studies demonstrated that depletion or reprogramming of certain subsets of stromal cells in solid tumors can disrupt the pro-tumorigenic niche and enhance endogenous and vaccine induced anti-tumor immunity[8-13]. One subset of CAFs that appear to be important in this process express the surface protease fibroblast activation protein (FAP)[14, 15]. Indeed, consistent with the hypothesis that this subset of stromal cells makes a significant contribution to the physical barriers and functional inhibition of anti-tumor immunity, we and others demonstrated that CAR T cells targeted to fibroblast activation protein (FAP-CAR T) expressing stromal cells can effectively inhibit tumor growth in mouse models of solid tumors[9, 11, 16]. Depletion of FAP^+ stromal cells was shown to inhibit tumor growth via immune-dependent and immune-independent mechanisms in a context-dependent manner related to tumor immunogenicity and the extent of

desmoplasia[9], however the mechanisms involved have not been defined. Moreover, in a recent study of lung cancer, a subpopulation of FAP^+ CAFs localized within the stroma that form multiple layers around tumor nests, were posited to play a role in T cell exclusion from tumor nests through deposition and alignment of matrix fibers[17]. The authors further posited that targeting of this subset of CAFs should enhance the efficacy of immunotherapy in the context of T cell-excluded tumors.

The role of tumor stroma as a critical component of TME that contributes to tumor growth and resistance to therapy is particularly striking in pancreatic ductal adenocarcinoma (PDAC), in which stroma can represent as much as >90% of the tumor volume and outcomes of any therapy remain dismal[13, 18-22]. The presence of distinct tumor nests has allowed the classification of the immune status of PDAC tumors toward a paucity of T cell infiltration (referred to as immune deserts) or accumulation of T cells in stroma-rich peri-tumoral regions but, excluded from tumor nests (referred to as immune exclusion). These peri-tumoral T cells are subject to immune suppression[22, 23] and this tumor exclusion phenomenon appears to contribute to the limited efficacy of adoptively transferred TAA-targeted CAR T cells[22, 24, 25].

In the current study, our goals were to use FAP-CAR T cells in PDAC models using real-time 2-photon imaging, immunohistochemistry, and flow cytometric analysis to: 1) define previously unknown mechanisms underlying the difference in efficacy of stromal cell- and TAA-targeted CAR T cells following intravenous administration into solid tumor-bearing mice; 2) test the hypothesis that the efficacy of TAA-targeted CAR T cells could be enhanced by first disrupting the TME with FAP-CAR T cells; and 3) determine if we could enhance the anti-tumor activity of endogenous T cells stimulated by anti-PD-1 antibodies by modifying the TME with FAP-CAR T cells. The data presented herein reveal three mechanisms that contribute to the efficacy of FAP-CAR T

cells, compared to TAA-targeted mesothelin (Meso)-CAR T cells, in inhibiting tumor growth. First is their capacity to eliminate FAP^+ stromal cells, thereby overcoming restriction of their extravasation and penetration of perivascular regions. Second is their capacity to deplete the desmoplastic peritumoral stroma resulting in reversal of immune exclusion and finally, their capacity to reprogram the immunosuppressive milieu, thus, rendering the TME permissive to TAA-directed endogenous T cell and adoptively transferred CAR T cell tumoricidal activity. In comparison, TAA-targeted Meso-CAR T cells were largely excluded from tumors and the few tumor-infiltrating Meso-CAR T cells detected were functionally suppressed in the context of intact stroma. Importantly, dual sequential treatment with FAP-CAR T cells overcame the negative effects of the TME on Meso-CAR T cells or immune checkpoint blockade in pre-clinical PDAC models, resulting for the first time in significant inhibition of tumor growth in multiple PDAC models by anti-PD-1 and by Meso-CAR_T cells. As FAP^+-CAFs are present in the majority of carcinomas, this study establishes a new strategy for potentiating immunotherapy in a wide variety of desmoplastic tumors based on initial disruption of the tumor stroma followed by TAA-CAR T cells or immune checkpoint blockade therapy (ICT) in settings in which they are poorly if at all effective as monotherapies.

Results

Comparable transduction efficiency, CAR expression and function of FAP- and Meso-CAR T cells *in vitro*

FAP is highly expressed in stroma of most carcinomas, including PDAC[9], and mesothelin is a promising TAA target expressed at high levels in PDAC (Extended Data Fig. 1a)[24, 26]. To compare the behavior of tumor stroma-targeted FAP-CAR T cells with

TAA (mesothelin)-targeted CAR T cells, we utilized a second-generation FAP-CAR vector encoding a scFv based on the sequence of the anti-FAP monoclonal antibody 4G5 produced in our laboratory[27] and a previously described mouse Meso-CAR designated A03[24] (Fig. 1a). Empty retroviral MigR vector-transduced T cells were used as a negative control[9, 11]. All 3 vectors encoded an IRES sequence followed by an enhanced green fluorescent protein (EGFP) cassette. The FAP and Meso CARs encoded 4G5 and A03 scFvs respectively, followed by a CD8 transmembrane/hinge sequence and 4-1BB and CD3ζ signaling domains (Fig. 1a). Mouse splenocytes were isolated, activated, and transduced with MigR control, Meso-CAR and FAP-CAR, consistently resulting in greater than 90% transduction efficiencies (Fig. 1b). Moreover, transduced MigR control, Meso-CAR and FAP-CAR T cells exhibited similar levels of proliferation following activation with anti-CD3/CD28 beads (Extended Data Fig. 1b). Flow cytometry analyses of the GFP^+ transduced T cells showed granzyme B (GzmB), tumor necrosis factor-α (TNF-α), and interferon-γ (IFN-γ) were also upregulated to a similar extent in the GFP^+ T cells transduced with MigR, Meso-CAR and FAP-CAR (Extended Data Fig. 1c). Finally, the chemokine, CXCL9, induced comparable transmigration of activated MigR control, Meso-CAR, and FAP-CAR T cells in a dual chamber migration assay (Extended Data Fig. 1d).

To compare the effector function of Meso- and FAP-CAR T cells *in vitro*, we assessed their cytolytic activities and IFN-γ release following co-culture with cells expressing their respective antigen targets, relative to their respective negative control targets. Specifically, Meso-CAR T cells were co-cultured with mesothelin-expressing parental 4662 PDAC cells or with mesothelin-knockout (KO) 4662 PDAC cells generated using *CRISPR/Cas9* system (Extended Data Fig. 1a), while FAP-CAR T cells were co-cultured with FAP-negative 3T3 fibroblasts or with 3T3 fibroblasts transfected to express

mouse FAP[11]. Meso-CAR T and FAP-CAR T cells exhibited comparable antigen- and dose-dependent cytotoxic activity (Fig. 1c) and IFN-γ release (Fig. 1d) *in vitro*.

Stromal-targeted FAP-CAR T cells inhibited PDAC tumor growth more effectively than Meso-CAR T cells *in vivo*

To compare the anti-tumor activity of FAP- and Meso-CAR T cells *in vivo*, we established subcutaneous 4662 PDAC tumors in syngeneic C57BL/6 mice. Mesothelin (Extended Data Fig. 1a) and FAP are highly expressed in 4662 tumor cells and tumor stromal cells, respectively[9]. To evaluate anti-tumor efficacy, we administered 5×10^6 FAP-CAR$^+$, Meso-CAR$^+$ and a comparable number of total MigR control T cells or PBS intravenously in mice when tumors reached a mean volume of 100-150 mm^3 (Fig. 1e). Compared with PBS or MigR control T cells, Meso-CAR T cells only minimally inhibited tumor growth and had no significant impact on survival of tumor-bearing mice. More robust inhibition of tumor growth and more prolonged survival was observed in tumor-bearing mice treated with FAP-CAR T cells (Figs. 1f-i and Extended Data Figs. 2a-b). Similar results were obtained in studies using the KPC genetically engineered mouse model (GEMM) that recapitulates tumor initiation, progression, and the genetic and histopathological characteristics of human PDAC[28]. KPC mice bearing spontaneous tumors of similar size, based on longitudinal non-invasive ultrasound imaging, were treated with 5×10^6 MigR control, Meso-CAR, and FAP-CAR T cells. In this model, we again saw only modest effects from the Meso-CAR T cells but observed more robust inhibition of tumor growth with the FAP-CAR T cells compared with MigR control and Meso-CAR T cells, monitored by non-invasive ultrasound imaging (Fig. 1j and Extended Data Figs. 2c-f). Median and overall survival were significantly extended by both Meso-CAR T and FAP-CAR T cells with a more profound effect observed in the FAP-CAR T cell treated cohort (Fig. 1k).

FAP-CAR T cells infiltrate and deplete their target cells more effectively than Meso-CART cells in PDAC tumors *in vivo*

Since FAP- and Meso-CAR T cells exhibited comparable functionality *in vitro,* we hypothesized that the greater anti-tumor activity of FAP-CAR T cells *in vivo* was at least partially due to their unique ability to overcome the physical barriers and immunosuppressive milieu imposed by FAP^+ stromal cells in the TME. To test our hypothesis, we utilized CD45.1 C57BL/6 mice as T cell donors to produce MigR control, Meso-CAR, and FAP-CAR T cells and adoptively transferred these cells via intravenous injection into CD45.2 C57BL/6 PDAC tumor-bearing hosts. Peripheral blood, spleens, and tumors were harvested to compare the trafficking, intra-tumoral localization and functionality of the adoptively transferred T cells *in vivo* at 1, 4 and 7 days post-T cell administration (Fig. 2a). Flow cytometry analyses revealed comparable accumulation of MigR control, Meso-CAR and FAP-CAR T cells in peripheral blood and spleens and the donor T cells in blood and spleen in each group expressed high levels of activation and proliferation markers, such as CD69 and Ki-67, and low levels of PD-1 (Extended Data Figs. 3a-b), indicative of good functionality of these T cells. These data suggest that all these T cells behave comparably in circulation.

In contrast, major differences were observed between tumor-infiltrating donor T cells from the different groups. Few $CD45.1^+GFP^+$ donor T cells infiltrated tumors in the MigR control and Meso-CAR T cell treated mice. In contrast, we observed significant time-dependent accumulation of $CD45.1^+GFP^+$ donor T cells in tumors starting as early as 1-day post-administration of FAP-CAR T cells and the tumor-infiltrating FAP-CAR T cells increased over time at least until 7 days post-administration (Fig. 2b and Extended Data Figs. 4a-c). In addition, on day 7, compared with MigR control and Meso-CAR T cells, tumor-infiltrating FAP-CAR T cells expressed lower levels of PD-1 (Fig. 2c), higher

levels of Ki-67 (Fig. 2d), and produced higher levels of IFN-γ (Fig. 2e) after isolation and *ex vivo* stimulation with a cell activation cocktail of PMA and ionomycin, in the presence of Brefeldin A to enhance intracellular accumulation of cytokines.

Flow cytometry of dissociated cells from tumors demonstrated the increase in FAP-CAR T cell infiltration over time correlated with a progressive reduction in FAP^+ cells (Fig. 2f [top and middle panels] and Extended Data Fig. 4d), whereas the reduction in $mesothelin^+$ cells was more modest and not evident until day 7 post-administration of FAP-CAR T cells (Fig. 2f [bottom panel] and Extended Data Fig. 4e), consistent with an indirect inhibition of FAP-CAR T cells on the growth and/or survival of FAP-negative tumor cells compared to their effect on FAP^+ stromal cells. Moreover, Meso-CAR T cells had no impact on FAP^+ cells at any time-point compared to MigR control T cells and only modestly reduced the proportion of $Mesothelin^+$ tumor cells and with more delayed kinetics, being evident only at day 7 compared to the more rapid impact of FAP-CAR T cells on the proportion of FAP^+ stromal cells at all time-points (Fig. 2f).

In parallel, we utilized multiplex-immunofluorescence (IF) to map the intra-tumoral localization of CAR T cells (GFP^+ cells) *in vivo* and to determine their spatial relationships with their respective FAP^+ stromal cell and $EpCAM^+$ tumor cell targets. In line with our flow data, we found accumulation of only rare MigR control and Meso-CAR T cells at days 1, 4 and 7 (Fig. 2g). In contrast, accumulation of FAP-CAR T cells was evident by day 4 and remarkably robust at day 7. In regions with more tumor-infiltrating FAP-CAR T cells, we found significant decreases in FAP^+ stromal cells and $EpCAM^+$ tumor cells (Fig. 2g) consistent with our prior studies demonstrating that FAP-CAR T cell-mediated depletion of stromal cells indirectly causes reduced proliferation and increased death of tumor cells[9].

Spontaneous tumors from KPC mice were also stained and showed an abundance of FAP$^+$ stromal cells surrounding PanCK$^+$ tumor cells (Fig. 2h). Staining done 7 days post-T cell injection showed the tumors to be devoid of GFP$^+$ CAR T cell infiltration in mice treated with MigR control and Meso-CAR T cells (Fig. 2h) which notably had no impact on either FAP$^+$ stromal cell or Mesothelin$^+$ tumor cells even by day 7 post-T cell administration. In contrast, we detected many GFP$^+$ FAP-CAR T cells infiltrating into the tumors, which diminished both FAP$^+$ stromal cells and PanCK$^+$ tumor cells (Fig. 2h), further validating the robust anti-tumor activity of FAP-CAR T cells in this autochthonous PDAC model.

Collectively, these results indicate that FAP-CAR T cells more readily traffic to, infiltrate and survive and/or expand in tumors compared to Meso-CAR T cells and that they more effectively deplete their target cells in syngeneic subcutaneous transplanted and autochthonous PDAC models *in vivo*. These data provide additional evidence that PDAC tumor progression is dependent on FAP$^+$ stromal cells and that targeting the stroma is sufficient to mediate a robust anti-tumor effect[9, 11]. Furthermore, these data directly demonstrate for the first time, that the differential efficacy *in vitro* and *in vivo* of FAP-CAR and Meso-CAR T cells reflects differences in their ability to infiltrate and remain functional in the TME.

Direct visualization of stromal-targeted FAP-CAR T cells, but not tumor antigen targeted Meso-CAR T cells, overcoming the stromal barrier and immunosuppressive microenvironment to infiltrate tumor nests

To better understand the distinct behaviors of stromal and TAA-targeted CAR T cells *in vivo*, we developed and optimized a precision-cut tumor slice-based real-time two-photon microscopy system. Briefly, mesothelin$^+$ 4662 PDAC cells were transduced with mCerulean3 (Extended Data Fig. 5a)[29] and were subcutaneously inoculated into

syngeneic mice and tumor-bearing mice were treated as described above. Tumors were harvested 1, 4 and 7 days post-administration of EGFP-expressing MigR control, Meso-CAR or FAP-CAR T cells. Tumors were cut into 500 µm slices using a vibratome. The slices were reacted with AF647-conjugated rat anti-mouse CD90.2 to label the stromal cells as described[30] and then immediately analyzed using real-time 2-photon microscopy (Fig. 3a). This *ex vivo* imaging system overcomes two intrinsic challenges of *in situ* live-imaging of PDAC tumors: (1) limited imaging depth resulting from dense stroma, and (2) breathing motion artifacts that limit intravital live imaging[25, 31, 32]. Importantly, we found that imaging tumor slices from treated mice within 1-2 hours of tumor harvest avoided complications in interpreting data obtained using more standard slice assays in which tumor slices are isolated from untreated mice and then treated *in vitro* and imaged over several days. Based on preliminary studies, we noted a robust wound-like response under the latter conditions. Therefore, our modified precision-cut tumor slice assay of tumors treated *in vivo* prior to harvest and harvested at different time-points post-treatment, better reflected the behavior of CAR T cells in the TME *in vivo*. Using this modified precision-cut tumor slice protocol, we performed systematic real-time 2-photon imaging of the impact of $EGFP^+$ CAR T cells treatment on $mCerulean^+$ tumor cells, AF647-CD90.2 labeled stromal cells, and matrix architecture based on label-free second harmonic generation (SHG) for fibrillar collagen, to image cell-cell and cell-matrix interactions in real-time in subregions of the TME including, the stromal-rich region surrounding tumor nests and within tumor nests per se.

Consistent with our flow and multiplexed-IF data, only rare GFP^+ MigR control and Meso-CAR T cells extravasated into the tumor site, even by day 7 post-administration (Figs. 3b-c). Moreover, the few donor T cells detected in these cohorts were restrained by abundant peritumoral stromal cells and fibrillar collagen network,

which restricted them from entering tumor nests (Fig. 3b), and they exhibited little, if any, stable interactions with stromal cells, matrix or tumor cells (Extended Data Movies 1-2) as evidenced by low levels of mean track speed (mean cell migration speed over 20 min), track straightness (ratio of cell displacement to the total length of the trajectory), and track length (total length of the trajectory) (Fig. 3d). In contrast, FAP-CAR T cells infiltrated and accumulated and exhibited robust motility within the stromal cell and collagen-rich regions surrounding tumor nests starting from day 1 and increasingly in tumors harvested from mice at days 4 and 7 post-treatment (Figs. 3b-c). Initially, FAP-CAR T cells, although highly motile, were restricted in their mobility and were largely confined by the stroma and prevented from entering tumor nests. Interestingly however, by day 4, and to much greater extent by day 7, after stromal cells and matrix were depleted, FAP-CAR T cells were found escaping from the confines of the stroma and successfully penetrating beyond the tumor borders into tumor nests (Fig. 3b and Extended Data Figs. 5b-d). Specifically, FAP-CAR T cells were often observed directionally migrating along remodeled thinner collagen fibers within the tumor nests (Fig. 3d and Extended Data Movies 3-4). Furthermore, FAP-CAR T cells by day 1-4 appeared activated with blast morphology and prominent uropods and were highly motile. These tumor-infiltrating FAP-CAR T cells exhibited relatively high levels of mean track speed and track length (Figs. 3d-e and Extended Data Movies 5-6).

As indicated by flow cytometry, multiplexed-IF, and real-time 2-photon microscopy, stromal cells were reduced to some degree as early as 1 day post-treatment with FAP-CAR T cells. Therefore, to better capture the earliest cell-cell and cell-matrix interactions of FAP-CAR T cells as they entered tumors, we performed similar analyses at earlier time-points. In these studies, we added AF647-anti-CD31 to the slices to image vasculature in addition to PE-CD90.2 to image stromal cells in slices

from mCerulean$^+$ 4662 tumor-bearing mice at baseline (prior to FAP-CAR T cell administration) and 6, 12, and 18 hours post FAP-CAR T cell administration. Interestingly, we observed a large number of extravasating GFP$^+$ FAP-CAR T cells surrounding peritumoral blood vessels (CD31$^+$ or CD31$^+$CD90.2$^+$) at 6 hours, which was further increased at 12- and 18 hours post-administration of FAP-CAR T cells (Extended Data Fig. 5e). Moreover, these FAP-CAR T cells started to crawl toward stromal cells (CD90.2$^+$), followed by their arresting in proximity to and forming stable interactions with these targeted stromal cells, presumably forming contacts due to engagement of their cognate antigen on FAP$^+$ stromal cells (Extended Data Fig. 5f and Movies 7-8). These data provide the first evidence that, in addition to an essential role in immune exclusion, FAP$^+$ stromal cells may also play a critical role in restricting T cell extravasation.

Stromal-targeted FAP-CAR T cells rapidly deplete matrix, enhance T cell infiltration and alter the immune and stromal landscapes

To characterize the longer-term impact of disruption of the fibro-proliferative response and matrix remodeling by FAP-CAR T cells, we performed multiplexed IF to spatially profile the stromal and immune landscape alterations in the TME in response to FAP-CAR compared to MigR control T cell or PBS treatments at 1 and 2 weeks post-treatment. Given the known heterogeneous nature of stromal cell subsets in the TME, we stained for FAP, alpha smooth muscle actin [α-SMA], platelet-derived growth factor receptor alpha [PDGFR-α] and/or podoplanin (PDPN). CAFs staining for all these markers were prevalent in tumors treated with PBS or MigR control T cells 1 week and 2 weeks prior (Fig. 4a, top row). In contrast, FAP$^+$-CAFs were selectively depleted in tumors from FAP-CAR T cells treated mice at 1 week post-treatment. However, by 2 weeks post-treatment with FAP-CAR T cells, other CAF subtypes were also depleted (Fig. 4a, top row). The depletion of stromal cells was unexpected found to be associated

with a rapid and profound loss of matrix, as evidenced by the marked decrease in remodeled collagen as detected by staining with collagen hybridizing peptide (CHP) that reacts with mechanically unfolded collagen molecules, and fibronectin (FN), at both 1 and 2 weeks post-FAP-CAR T cells treatment (Fig. 4a, middle row). Tumors from PBS and MigR treated mice were largely devoid of $CD3^+$T cells at both 1 and 2 weeks post-treatment, while the reduction in stromal cells and matrix observed in the tumors from FAP-CAR T cell-treated mice was associated with significant infiltration of $CD3^+$ T cells at 1 week that further increased at 2 weeks post-treatment when Pan-CK+ tumor cells were reduced (Fig. 4a, bottom row).

We next analyzed the overall immune profile of tumors by multiparametric flow cytometry (Extended Data Fig. 6). Consistent with the IF data above, flow cytometric analysis of dissociated tumors performed in parallel demonstrated efficient infiltration of FAP-CAR T cells compared with MigR control T cells (Fig. 4b). Endogenous lymphocyte and myeloid cell content in the tumors 1 week post-administration of FAP-CAR, MigR control T cells or PBS were comparable. In contrast, by 2 weeks post-treatment, tumors from FAP-CAR T cells treated mice exhibited greater infiltration/accumulation of endogenous $CD3^+$ T cells, especially $CD8^+$ T cells, and NK cells along with decreased accumulation of granulocyte-like myeloid cells ($CD11b^+Ly6C^{lo}Ly6G^+$) (Fig. 4b). Taken together, these data support the idea that FAP-CAR T cells can deplete stromal cells and matrix and substantially modify the immune contexture of the TME by recruiting cytotoxic effector lymphocytes and excluding or killing potentially immunosuppressive myeloid cells.

Ablation of FAP^+ stromal cells by FAP-CAR T cells enhances the efficacy of immune checkpoint blockade therapy

PD-L1 can be expressed on tumor cells and myeloid cells and, after binding to PD-1 expressed on activated T cells, can induce immunosuppression. Thus, blockade of the PD-L1/PD-1 pathway has been found to enhance anti-tumor immunity and inhibit tumor growth in preclinical studies and in clinical trials for many types of cancers. However, in PDAC, checkpoint blockade has generally been disappointing. This is likely due, at least partially, to the lack of infiltration of effector immune cells in the TME that we validated in the experiments described above. Accordingly, we investigated whether FAP-CAR T cells could enhance the efficacy of treatment with anti-PD-1 in PDAC tumors.

4662 tumor-bearing CD45.2 C57BL/6 mice were treated with either FAP-CAR or MigR control T cells (CD45.1). Four days post-T cell administration, the mice were given isotype control antibody (IgG) or anti-PD-1 antibody twice weekly by intraperitoneal injection. This resulted in 4 experimental groups of mice that received either FAP-CAR T cells and IgG, FAP-CAR T cells and anti-PD-1, MigR control T cells and IgG, or MigR control T cells and anti-PD-1 (Fig. 5a). Consistent with previous reports, anti-PD1 antibodies had no effect on tumor growth. As above (Fig. 2b), there was significant slowing of the tumors by FAP-CAR T cells. However, the combination of FAP-CAR T cells followed by anti-PD-1 synergistically reduced tumor growth and prolonged survival compared with other treatment combinations (Figs. 5b-e). Flow cytometry and multiplex IF analyses confirmed the depletion of FAP^+ stromal cells and blockade/neutralization of PD-1 on T cells (Figs. 5f-h). With regard to T cells, we found a significantly greater intra-tumoral accumulation of FAP-CAR T cells when combined with anti-PD-1 (Fig. 5f). Importantly, our data shows that FAP-CAR T cells combined with anti-PD-1 therapy facilitated the recruitment of endogenous $CD8^+$ T cells (Figs. 5f-h). Moreover, anti-PD-1 dramatically improved the functionality of cytotoxic $CD8^+$ T cells, as evidenced by the

down-regulation of co-inhibitory markers such as Tim-3 and the enhancement of TNF-α and IFN-γ expression upon restimulation *ex vivo* (Fig. 5i). Collectively, these data demonstrate that FAP-CAR T cells enhanced the efficacy of anti-PD-1 therapy in controlling tumor growth.

FAP-CAR T cells are sufficient to convert a hostile tumor milieu to render PDAC tumors permissive to TAA-CAR T cells and endogenous immune cell infiltration and tumoricidal activity

Although pre-treatment of FAP-CAR T cells followed by anti-PD-1 therapy showed enhanced inhibition of PDAC tumor growth, the overall survival was only modestly improved, thus warranting investigation of other combination therapies. We next investigated whether FAP-CAR T cells can augment anti-tumor immunity of subsequent administration of Meso-CAR T cells. Accordingly, 4662 tumor-bearing syngeneic mice were first treated with MigR, Meso-CAR or FAP-CAR T cells. Two weeks later, mice treated with MigR control T cells received a second dose of MigR control T cells and mice treated with Meso-CAR T cells were given a second treatment with either MigR control T cells or Meso-CAR T cells. In parallel, the mice initially treated with FAP-CAR T cells received a second treatment with either MigR control, Meso-CAR, or FAP-CAR T cells (Fig. 6a). Dual doses of Meso-CAR T cells had no significant effect on the growth of tumors compared to either dual doses of MigR control T cells or Meso-CAR T cells followed by MigR control T cells. Interestingly, we found that dual doses of FAP-CAR T cells not only slowed growth of the tumors but initially induced a degree of tumor regression compared to tumors in mice that received a first dose of FAP-CAR T cells with a subsequent dose of MigR control T cells. However, most notably, the combination of FAP-CAR and subsequent Meso-CAR T cells showed the strongest inhibitory effect on tumor growth and tumor burden (Figures 6b-c and Extended Data

Figs. 7a-c) and had the greatest effect on survival (Fig. 6d). Importantly, pre-treatment of FAP-CAR T cells followed by Meso-CAR T cells also robustly inhibited and stabilized the tumor growth of autochthonous KPC (Figs. 6e-g) and completely regressed the tumors in AsPC-1 (Figs. 6h-j) and Capan-2 (data not shown) human PDAC xenograft models, exhibiting high translational potential of our combination strategy in clinic.

To explore mechanistically how FAP-CAR T rendered PDAC tumors sensitive to Meso-CAR T cells, we performed multiplex IF analysis. This analysis demonstrated consistent depletion of CAFs and matrix by FAP-CAR T cells compared to the tumors first treated with MigR control or Meso-CAR T cells (Extended Data Figs. 7d-e). Moreover, a higher number of total T cells accumulated in tumor nests accompanied by significantly decreased expression of PanCK$^+$ tumor cells and depletion of PDPN$^+$ CAFs in the tumors treated with FAP-CAR T cells followed by FAP-CAR and Meso-CAR T cells than in other combinations (Extended Data Figs. 7d-e). Notably, FAP-CAR T cells combined with subsequent Meso-CAR T cells significantly increased apoptosis and suppressed proliferation of tumor cells, as evidenced by up-regulated cleaved caspase-3 and down-regulated Ki-67 on tumor cells (Fig. 6k). Furthermore, we found that pre-treatment with FAP-CAR T cells reduced the proportion of TGF-β producing cells and intra-tumoral angiogenesis, especially when combined with subsequent administration of a second dose of FAP-CAR T cells or Meso-CAR T cells (Fig. 6k). Flow cytometry analyses of tumors at the endpoint further confirmed the reduction in TGF-β$^+$ cells, which reflected the decrease in the number of α-SMA$^+$ CAFs and myeloid cells, the main sources of TGF-β secretion (Extended Data Fig. 7f).

To test our hypothesis that FAP-CAR T cells can enhance the trafficking, infiltration, and functionality of subsequently administered Meso-CAR T cells, CD45.2 C57BL/6 mice were utilized as donors to produce EGFP-tagged MigR control, Meso-

CAR, and FAP-CAR T cells, and these T cells were adoptively transferred via intravenous injection into CD45.1 C57BL/6 mCerulean labelled PDAC tumor-bearing hosts. 4 days post-administration of the first treatment, these mice were treated with tdTomato-tagged Meso-CAR T cells which were derived from tdTomato mice and transduced to express mouse Meso-CAR without the GFP fluorescence tag as the second treatment. 2-photon microscopy, multiparametric flow cytometry, and multiplexed IF were performed at day 1, 4 and 7 post second treatment (Fig. 7a). Under these conditions, exogenous (CD45.2) and endogenous (CD45.1) T cells, as well as the first (EGFP) and second (tdTomato) dose of CAR T cells could be distinguished and characterized. Consistent with our previous results described above, we found significantly more GFP^+ FAP-CAR T cells accumulated in both stromal cell-rich and tumor nest regions at day 1, 4 and 7 post-second treatment compared with GFP^+ MigR control and Meso-CAR T cells, resulting in the rapid ablation of FAP^+ stromal cells and $mesothelin^+$ tumors cells (Figs. 7b-c and Extended Data Figs. 8a-b). Dramatically increased numbers of $tdTomato^+$ Meso-CAR T cells started to infiltrate into both tumor stroma and tumor nest regions, even at day 1 post-second treatment in tumors first treated with FAP-CAR T cells compared with the tumors first treated with MigR control or Meso-CAR T cells (Figs. 7b-c). Moreover, these $tdTomato^+$ Meso-CAR T cells infiltrated and accumulated in tumor nests in a time-dependent manner with profound depletion of $mCerulean^+$ tumor cells over time (Figs. 7b-c and Extended Data Movies 9-10). Real-time 2-photon microscopy confirmed that the first treatment of FAP-CAR T cells rendered tumors permissive to Meso-CAR T cells allowing their extravasation, infiltration of and function within tumor nests. Flow cytometry and multiplex IF analyses further confirmed that the number of $CD45.2^+tdTomato^+$ Meso-CAR T cells in tumors first treated with FAP-CAR T cells were significantly higher than those treated with MigR control and Meso-CAR T cells (Fig. 7d, Extended Data Figs. 8c-d). Also important was

the observation that a first dose of FAP-CAR T cells enhanced the activation of CD45.2$^+$tdTomato$^+$ Meso-CAR T cells in tumor sites, as demonstrated by increased expression of GzmB, TNF-α, and IFN-γ after stimulation (Fig. 7e). Collectively, these data suggest that ablation of FAP$^+$-CAFs by FAP-CAR T cells have translational potential for enhancing the efficacy of Meso-CAR T cell therapy, and likely other TAA targeted therapies, in solid tumors.

Sequential administration of FAP-CAR T cells with Meso-CAR T cells enhances systemic endogenous adaptive anti-tumor immunity in PDAC models

The data above indicates that the combination of FAP- and Meso-CAR T cells enhanced the anti-tumor activity of Meso-CAR T cells. Moreover, we found FAP-CAR T cells enhanced the anti-tumor activity of anti-PD-1 suggesting that FAP-CAR T cells alone may have an inherent capacity to modulate the endogenous immune landscape. Therefore, to address if the changes in the TME induced by the combination of FAP- and Meso-CAR T might have the potential to engage endogenous anti-tumor immunity, 4662 tumor-bearing C57BL/6 were pre-treated with MigR control or FAP-CAR T cells. 2 weeks later, the mice receiving MigR control T cells were treated with a second dose of MigR control T cells, whereas the mice given first dose of FAP-CAR T cells received a second treatment of MigR control, FAP-CAR, or Meso-CAR T cells (Fig. 8a). Consistent with our data above (Fig. 6b), we found pre-treatment of FAP-CAR T cells significantly enhanced the efficacy of the second treatment with Meso-CAR T cells in inhibiting tumor growth (Extended Data Fig. 9a). Based on flow cytometry, we found that FAP-CAR T cells followed by subsequent Meso-CAR T cells treatment increased the infiltration of endogenous CD8$^+$ T cells in the tumor sites and a concomitant decrease in CD4$^+$FoxP3$^+$ Treg cells (Fig. 8b and Extended Data Figs. 9b-c) and increase in IFN-γ expression in endogenous CD8$^+$ T cells after restimulation compared to other combinations (Fig. 8c).

The combination of FAP-CAR and Meso-CAR T cells also led to the strongest activation of endogenous splenic $CD8^+$ T cells, as demonstrated by the high levels of expression of IFN-γ after restimulation (Fig. 8c). Moreover, in addition to the decreased levels of Ly-$6C^+$Ly-$6G^+$ myeloid cells and F4/$80^+$$CD206^+$ tumor-associated macrophages (TAMs) (Fig. 8d Extended Data Figs. 9d-f), we found that the rare conventional dendritic type 1 cells (cDC1, $CD45^+$$CD103^+$$CD11c^+$) subpopulation, which plays a central role in the adaptive immune response by cross-presenting antigen to cytotoxic $CD8^+$ T cells, was significantly increased in the tumors treated with FAP-CAR T cells and Meso-CAR T cells (Fig. 8e), indicating that the mobilization of endogenous $CD8^+$ T cells might be facilitated by the presence of cross-presenting cDC1s. Multiplexed IF analyses also validated the increase in endogenous $CD8^+$ T cells (especially IFN-$\gamma^+$$CD8^+$ T cells) and cDC1, and indicated that potentially immune suppressive cells, such as TAMs (especially $CD206^+$ M2 macrophages) and Treg cells were excluded (Fig. 8f). Collectively, these data indicate that the immune-desert/excluded TME of PDAC was reprogrammed by the combination of FAP-CAR and Meso-CAR T cells. Together, these results suggest that the combination of FAP-CAR and Meso-CAR T cells treatment can also promote endogenous adaptive anti-tumor immunity.

Discussion

Whereas tumor antigen targeted (TAA) CAR T cells have shown remarkable success in treating some hematopoietic cancers, extending this innovative immunotherapeutic approach to the treatment of solid tumors has proven challenging, at least partially due to limited tumor infiltration, penetration, and loss of functionality within the solid tumor microenvironment. However, in-roads have been made in pre-clinical models of solid tumors using stromal cell-targeted, FAP-CAR T cells in multiple tumor

types[9, 11]. Notably, FAP-CAR T cells have shown significant efficacy even in the highly desmoplastic KPC syngeneic transplant and autochthonous GEMM models of PDAC[9, 11] in which the tumor antigen mesothelin-targeted CAR T cells have very modest, if any effect[24, 26, 33]. Therefore, we used these models to define mechanisms that underly the dichotomy between the impact of TAA- versus stromal cell-targeted CAR T cells in solid tumors. The data presented herein, demonstrate that FAP^+ stromal cells and associated matrix contribute to a microenvironment that minimizes recruitment and mediates immune exclusion and immunosuppression of Meso-CAR T cells. In contrast, FAP-CAR T cells, by ablating FAP^+ stromal cells and by remodeling matrix as they eliminate CAFs, overcome the hostile TME and thereby successfully extravasate into tumors and eventually infiltrate into tumor nests. As previously reported, this results in indirect tumor cell death and partial inhibition of tumor growth[9, 11]. In this study, we demonstrate that these effects of FAP-CAR T cells are sufficient to convert a hostile tumor milieu to become permissive to TAA-CAR T cells and endogenous immune cell infiltration and tumoricidal activity, thus resulting in enhanced activity when given in combination with Meso-CAR T cells or anti-PD-1 in our pre-clinical models of PDAC tumors, and our previously reported data in combination with a tumor vaccine in a more immunogenic mouse model of lung cancer[11]. These results provide a strong rationale for translating combinations of stromal cell-targeted and TAA-targeted therapies or ICT to patients.

This study also provides novel mechanistic insights into the roles of stromal cells and matrix in severely limiting the impact of various tumor cell-directed immunotherapies in the context of solid tumors and how stroma-dependent hinderance of anti-tumor immunity can be overcome at an unprecedented resolution based on real-time tumor slice-based two-photon microscopy to define cell-cell and cell-matrix interactions *in situ*. By directly comparing the spatiotemporal behavior of Meso-CAR and FAP-CAR T cells

within live PDAC tissues at various time points post-T cell administration to tumor-bearing mice, we found FAP-CAR T cells have an advantage at several levels. First, FAP-CAR T cells exited the circulation and traversed the perivascular regions in greater numbers and more rapidly than Meso-CAR T cells. This is consistent with the presence of FAP^+ perivascular cells that likely impede Meso-CAR T cells[34], while these cells are likely eliminated by FAP-CAR T cells that can then continue their intra-tumoral migration. Second, we found that a stromal cell and matrix-dense network surrounding tumor nest more effectively trapped and limited Meso-CAR and MigR control T cells for a more prolonged period thus deterring their penetration of the stromal border and preventing their direct contact with tumor cells compared to FAP-CAR T cells, a phenomenon referred to as immune exclusion. As the stromal border was found to be rich in FAP^+ cells[17], this again is likely due to the ablation of these FAP^+-CAFs cells that elaborate and align fibrillar matrix as they come into contact with their target in tumor border region. Third, tumor-infiltrating Meso-CAR and MigR control T cells lost functionality as manifested by morphologic features of inactivated T cells and poor motility, their exhausted phenotypes (low Ki-67 and IFN-γ) characterized by flow cytometry, and their lack of anti-tumor activity. By contrast, stromal-targeted FAP-CAR T cells exhibited blast morphology and prominent uropods typical of activated T cells and efficiently trafficked to and remained functional as the result of their ability to deplete immunosuppressive FAP^+ stromal cells and matrix. We also found the strong enrichment of IFN-γ^+ FAP-CAR T cells at tumor sites, suggesting T cell activation and cytokine secretion within the tumor also supported their sustained activation.

Importantly, we could observe the dynamics of the cytolytic activity of FAP-CAR T cells *ex vivo* in precision-cut tumor slices. After extravasation from blood vessels, as early as 12-16 hours post their intravenous administration, we observed FAP-CAR T

cells encountering stromal cells leading to their transient arrest in apparent contact with their targets and formation of immune synapses followed by target cell death. Loss of targeted stromal cells, particularly at the tumor border at later time points, was notably associated with nearly complete clearance of fibrillar collagen by 1 week post-FAP-CAR T cell administration, as indicated by the loss of SHG signal and as confirmed by IHC. This remodeling of fibrillar matrix was likely the result of depletion of stromal cells responsible for depositing matrix and possibly an increase in remodeling enzymes. However, the dramatic and rapid kinetics of the loss of matrix leads us to speculate that stromal cells, through their impact on matrix architecture and the physical tension they impose on matrix fibrils, may also protect against proteolytic degradation and turnover of matrix and that ablation of stromal cells therefore further promotes matrix degradation and turnover. Future studies will address this hypothesis. In any case, disruption of the stromal network was associated with resumption of FAP-CAR T cell motility and a significant number of FAP-CAR T cells successfully traversing the tumor border and entering into the tumor nests where they were often observed directionally migrating along thinner elongated collagen fibers within the tumor nests. Repeated cycles of "motility" and "arrest/target-cell interactions" of FAP-CAR T cells resulted in their time-dependent advancement deeper into tumor nests.

It is important to note that CAFs are heterogeneous, with FAP expressed on a prominent subset, but not all CAFs. Another well-characterized subset of CAFs, referred to as myCAFs, express αSMA. FAP^+ and $αSMA^+$ subsets of CAFs are phenotypically and functionally distinct but overlapping in the context of PDAC[9, 35-39]. In a recent study of CAF gene expression signatures, and validated at the protein level, $FAP^+αSMA^+$ double positive cells were reported to be highly represented amongst the multi-layered CAF-rich stromal network surrounding tumor nests and mediating immune exclusion in PDAC[17].

Furthermore, the diversity of CAFs is dependent on the heterogeneity of their progenitors and further driven by environmental factors, such as growth factors, including TGFβ and cytokines (such as IL-1 and LIF), the latter of which for example, preferentially drive the generation of CAFs with gene signatures implicating them in inflammation[32, 38, 40], as well as matrix composition, stiffness and tension of substratum[41-44]. These subsets can also exhibit plasticity, with gene expression and phenotype varying as a function of substratum and soluble factors and can undergo epigenetic reprograming to reinforce their state [38, 41]. Expectedly, and consistent with prior reports, we found that FAP^+ cells were initially selectively depleted up to one week post-administration of FAP-CAR T cells with little impact on prevalence of αSMA^+ cells. However, somewhat surprisingly, a significant depletion of αSMA^+ CAFs became evident by two weeks post-treatment with FAP-CAR T cells. There are several, not mutually exclusive, explanations for this observation, including, that αSMA^+ cells may derive from FAP^+ progenitors that once depleted are no longer available as a reservoir to maintain the αSMA^+ population. This is, however, unlikely the sole explanation since we noted that FAP^+ cells can be replenished over time[9]. Another possibility is that the majority of αSMA^+ cells that are eventually depleted also express lower levels of FAP and that loss of $FAP^{hi}\alpha SMA^{lo}$ cells are depleted more readily and earlier, followed over time by depletion of $FAP^{lo}\alpha SMA^{hi}$ CAFs. In addition, as previously posited[41, 43], FAP^+ cells may mediate early matrix remodeling leading to the generation of a collagen-rich and increasingly stiff matrix that is required for the generation of αSMA^+ CAFs, such that the loss of FAP^+ cells leads to modifications of matrix that can no longer sustain αSMA^+ CAFs. We further demonstrated that the level of TGF-β, which is critical in translating signals from ECM and/or stiffness to initiate and facilitate the fibrotic process and immunosuppression[45, 46], were down-regulated by FAP-CAR T cells administration,

partially supporting the broad remodeling of fibrotic TME, including stromal cells, ECM and even stiffness.

We previously reported that, in addition to the immune-independent growth inhibitory effects conferred by reduction in stromal-dependent pro-tumorigenic signals, FAP-CAR T cells also inhibited growth of multiple tumor types through immune-dependent mechanisms and enhanced the efficacy of a tumor antigen vaccine in a mouse model of lung cancer. In the current study, we present detailed analysis of the impact of FAP-CAR T cell-mediated depletion of the stromal network on the immune landscape that has important implications for clinical translation. Specifically, we demonstrate that treatment with FAP-CAR T cells renders the TME permissive to the infiltration and cytolytic function of adaptively transferred TAA-directed Meso-CAR T cells, as well as enhancing endogenous tumor immunity in the context of immune checkpoint therapy with anti-PD-1. Notably, treatment with FAP-CAR T cells resulted in increased recruitment of cytotoxic effectors ($CD8^+$ T and NK cells) and decreased the number of immunosuppressive myeloid cells, which was associated with down-regulated TGF-β signaling. FAP^+-CAFs also secrete the CXC-chemokine ligand 12 (CXCL12) that hinders T cell recruitment and chemokine ligands CCL2, CCL3, CCL4, and CCL5[8, 47] that recruit myeloid cells. Thus, depletion of FAP^+-CAFs by FAP-CAR T cells can also promote intra-tumoral infiltration of T cells by impairing the CXCL12-CXCR4 axis and down-regulating chemokines that influence myeloid cells recruitment into the TME[47]. Moreover, as CAFs reportedly can compete metabolically with T cells, FAP-CAR T cells also likely alter the metabolic status of the TME in favor of endogenous anti-tumor immunity and functionality of adaptively transferred CAR T cells[48]. Finally, CAFs can also produce hepatocyte growth factor (HGF), which further activates its cognate receptor, c-Met, on tumor cells resulting in a pro-tumorigenic environment by triggering

invasive and metastatic behavior on tumor cells[49, 50]. As such, the broad depletion of stromal cells by FAP-CAR T cells may induce the reduction of tumor-enhancing growth factors including HGF and c-Met, thus limiting the proliferation and invasiveness of cancer cells.

Combinatorial therapies with TAA-CAR T cell therapy and ICT are being pursued in the clinic. However, such combinations are predicted only to be successful if sufficient numbers of TAA-CAR T cells penetrate surrounding stroma to gain access to their target tumor cells; to date, ICT has proven to have little impact on CAR T cell-mediated tumor growth control[51]. In contrast, we found that pre-treatment with stromal cell-targeted FAP-CAR T cells had additive to synergistic effects when followed by PD-1 blockade. The abundance of both exogenous (FAP-CAR T cells) and endogenous T cells, mainly $CD8^+$ T cells, increased after a combination of FAP-CAR T plus PD-1 immune checkpoint blockade. Importantly, these endogenous $CD8^+$ T cells proliferated, produced TNF-α and IFN-γ upon stimulation, and expressed lower levels of Tim-3, indicating that FAP-CAR T cells in combination with anti-PD-1 overcame suppression of the infiltrating endogenous T cells. Although these results, together with previous studies that showed depletion of FAP^+-CAFs enhanced the efficacy of anti-cytotoxic T lymphocyte associated protein 4 (CTLA-4) and programmed cell death ligand 1 (PD-L1) blockade[8] and prolonged survival, the response was transient with resumption of tumor growth and demise of all animals in time. Promisingly, we found a combination of FAP-CAR T cells followed by Meso-CAR T cells had a more robust effect with tumor stabilization and even regression observed in some PDAC-bearing mice that translated into greater prolongation of survival. Based on real-time 2 photon microscopy, the efficacy of this combination corresponded to the efficient recruitment of Meso-CAR T cells to tumor site and their successful penetration of tumor nests subsequent to depletion of the surrounding stroma in response to pre-

treatment with FAP-CAR T cells. Moreover, tumor-infiltrating Meso-CAR T cells arrested in proximity to their tumor cell targets and exhibited a blast-like morphology and prominent uropods, reflecting an activated state as the result of encountering tumor cells. Furthermore, the Meso-CAR T cells that infiltrated tumors in mice first treated with FAP-CAR T cells produced high levels of cytokines, including TNF-α and IFN-γ, and GzmB, inducing effective killing of tumor cells. As a result, the combination of FAP-CAR followed by Meso-CAR T cell treatment, induced a dramatic diminution in proliferating cancer cells and increased cancer cell apoptosis. Of interest, we also observed activation of endogenous $CD8^+$ T cells in the tumor site and spleens and an abundance of cDC1, suggestive of systemic improvement of adaptive anti-tumor immunity. In a single other study of a nascent lung metastasis model, Kakarla et al[16] found that combining FAP-specific T cells with T cells that targeted the EphA2 antigen on A549 cancer cells themselves, enhanced overall anti-tumor activity and conferred a survival advantage compared to either alone. However, there are several notable differences in the design of that study compared to that reported here. First, whereas we treated mice with established tumors, in their study A549 tumor cells were intravenously injected and then received treatment just 4 days post-tumor cell inoculation, prior to generation of established tumors. Secondly, their study was conducted exclusively in a single human tumor xenograft model in immune incompetent mice, whereas we evaluated the impact of the dual treatment in two xenografts models as well as a syngeneic transplant and an autochthonous PDA model in immune competent animals.

In conclusion, our results provide promising data to support the development of combinatorial approaches including stromal cell and tumor antigen targeted immunotherapies for translation to the clinic in the setting of highly desmoplastic cancers.

Methods

Animals

C57BL/6J (CD45.1 donor and CD45.2 recipient), NOD/SCID/IL2-receptor γ chain knockout (NSG) and B6.129(Cg)-*Gt(ROSA)26Sor*$^{tm4(ACTB\text{-}tdTomato,\text{-}EGFP)Luo}$/J (mT/mG) mice were purchased from Jackson Laboratory. Fully backcrossed *Kras*^{G12D};*Trp53*^{R172H};*Pdx-1-Cre* (KPC) C57BL/6 mice were bred and maintained in our institution. All animal experiments were approved by the Institutional Animal Care and Use Committee (IACUC) of the University of Pennsylvania and were carried out in accordance with the guidelines. Mice were housed in a specific pathogen-free (SPF) condition (12 h light/12 h dark cycle, 20-25°C) and had free access to water and chow. Animal health status was routinely checked by qualified veterinarians.

Female mice aged 8-10 weeks were used unless indicated otherwise. For all animal work, mice with similar age and weight were randomized before tumor inoculation. Prior to further treatment, the tumor-bearing mice were randomized with respect to their tumor sizes to ensure all treatment groups had equivalent tumor burden before treatment. All animal experiments were performed in the same well-controlled pathogen-free facility with the same mouse diets.

Cell lines

Human CCD-19 lung fibroblast (CCD19-Lu), human AsPC-1 and Capan-2 PDAC tumor cells, human 293T cells and Phoenix-ECO packaging cells were purchased from ATCC. Mesothelin-positive 4662 cells were established from the fully backcrossed C57BL/6J KPC PDAC mouse model and kindly provided by Dr. Robert H. Vonderheide (University of Pennsylvania)[9]. 3T3.mFAP.GFP/Luc expressing high level of FAP and 3T3.GFP/Luc without FAP expression cells were generated by transduction with the lentivirus of firefly

luciferase as previously described[11]. All cell lines were tested for the presence of mycoplasma contamination (MycoAlert Mycoplasma Detection Kit, Lonza). For Cerulean labeling, 4662 PDAC cells were transduced with mCerulean retrovirus (Addgene# 96936)[29] to generate mCerulean^{+} 4662 PDAC cells and mCerulean^{hi} cells were sorted. Mesothelin knock-out 4662 cell line was generated by using *CRISPR-Cas9* system. Briefly, the gRNA oligonucleotides against murine mesothelin (5'-ATGTGGATGTACTCCCACGG-3') (synthesized by Dr. Genewiz, MA, USA) were cloned into lentiCRISPRv2 hygro vector (Addgene# 98291) as previously reported[52]. The plasmids were then packaged into lentiviral particles using 293T cells. 4662 cells were infected with lentivirus and selected by 250 µg/ml Hygromycin B for a week. Single cell clones were isolated using limited dilution and finally identified by western blot and flow cytometry. All cancer cells were cultured at 37°C with 5% CO_2 in DMEM including 10% heat-inactivated Fetal Bovine Serum (FBS), 100 U/ml penicillin-streptomycin and L-glutamine. Phoenix packaging cells (ATCC) were maintained at 37°C with 5% CO_2 in RPMI-1640 including 10% heat-inactivated FBS, 50 U/ml penicillin-streptomycin and L-glutamine. CCD-19 lung fibroblasts were cultured at 37°C with 5% CO2 in MEM including 10% heat-inactivated FBS, sodium pyruvate, non-essential amino acids, 50 U/ml penicillin-streptomycin and L-glutamine.

METHOD DETAILS

Vector generation, T cell isolation and expansion, and generation of CAR T cells

The second-generation anti-mouse mesothelin A03 CAR retroviral construct, which included anti-mouse mesothelin scFv, mouse CD8α hinge, CD8α transmembrane domain, mouse 4-1BB costimulatory domain, mouse CD3ζ signaling domain and EGFP reporter, was generated as previously reported[24]. The anti-human mesothelin M11 scFv was generated from a human phage display library and selected for its ability to bind to

purified human mesothelin. The VH and VL variable domains of the M11 scFv were fused with a human CD8α hinge, CD8α transmembrane domain, and two cytoplasmic domains derived from 4-1BB and CD3ζ. This anti-human Meso-CAR M11 was subcloned into the MigR1 retroviral vector, which also expresses EGFP, using an internal ribosomal entry site (IRES) as we have previously describe[53]. The second-generation anti-FAP CAR construct was generated by cloning the 4G5 scFv followed by human CD8α hinge, CD8α transmembrane domain, 4-1BB costimulatory domain and CD3ζ signaling domain into the MigR1 retroviral backbone, upstream of IRES and EGFP[27]. This CAR targets both human and murine FAP.

Mouse T cells were isolated from the spleen with T cell isolation kit (STEMCELL) according to the manufacturer's instructions. T cells were stimulated with Dynabeads Mouse T-Activator CD3/CD28 beads (Gibco) for 48 hours and were separated from beads prior to transduction. Infective particles were generated from the supernatants of Phoenix-Eco cells transfected with the retroviral vector plasmid and helper plasmids using Lipofectamine 2000 (Invitrogen) as we have previously described[9, 11, 54]. Indicated retroviruses were added into RetroNectin (20 mg/mL, Takara) pre-coated untreated 24-well plate and spun down at 1000g for 1 hour. Activated T cells were transduced with retroviruses at MOI of 3000 for 48 hours. Transduction efficiency was calculated based on expression of anti-mesothelin or anti-FAP CAR, assessed by staining with APC $F(ab'_2)$ fragment goat anti-human (Meso-CAR) or mouse (FAP-CAR) IgG (Jackson ImmunoResearch) respectively, and EGFP expression using flow cytometry.

Cytotoxicity and cytokine release assay

For checking the cytotoxicity of FAP-CAR T cells *in vitro*, 3T3.GFP/Luc and 3T3.mFAP.GFP/Luc cells were co-cultured with untransduced (UTD), MigR or FAP-CAR T cells at the E:T ratios of 1:1, 5:1 and 10:1, in triplicate, in 96-well round-bottomed

plates. After 18 hours, the culture supernatants were collected for IFN-γ analysis using an ELISA (Mouse IFN-γ Quantikine ELISA Kit, R&D System). The cytotoxic ability of FAP-CAR T cells was determined by detecting the remaining luciferase activity from the cell lysate using Luciferase Assay System (Promega) by measuring relative light unit (RLU). For checking the cytotoxicity of Meso-CAR T cells, 4662 mesothelin KO and parental 4662 PDAC cells were co-cultured with UTD, MigR or Meso-CAR T cells at the same E:T ratios as indicated above. Following an overnight co-incubation of T cells and target cells, supernatants were collected to quantify IFN-γ release by the same ELISA kit, and target cell viability was assessed using CellTiter 96 Aqueous Non-Radioactive Cell Proliferation Assay (MTS; Promega) by measuring the absorbance at 570 nm. In these killing assays, target cells alone were set as negative control to detect spontaneous death, and target cells lysed with water were set as positive control to get the maximal killing. The percentage of killing was calculated using the formula: % lysis = 100 × (spontaneous death - tested sample readout)/(spontaneous death - maximal killing).

CAR T cell transmigration assay

For transwell assays, the bottom wells were filled with 600 µl of T cell media with or without 100 ng/ml murine CXCL9 (Peprotech). 5×10^5 activated MigR control, Meso-CAR or FAP-CAR T cells were suspended in 100 µl T cell media and plated on the upper chamber of the transwell with 3 µm pore size filters (Millipore). After 4 hours of incubation at 37 °C, migrated T cells collected from the bottom wells were quantified using a cell counter.

Tumorigenesis and CAR T cell treatment studies

For syngeneic subcutaneous tumor model, 4662 or mCerulean$^+$ 4662 (3×10^5) PDAC cells were suspended into 100 mL PBS and s.c inoculated into right flank of C57BL/6

mice. For human xenograft subcutaneous tumor model, human AsPC-1 or Capan-2 (0.5 × 10^6) PDAC cells were co-injected with CCD-19 human lung fibroblasts (1.5 × 10^6) were suspended into 100 μL PBS and s.c inoculated into right flank of NSG mice. Tumor size was measured three times per week using caliper. Tumor volume was calculated as width × width × length × 0.5. The treatments started when the tumor volume reached 100-150 mm^3 in C57BL/6 mice or 50-100 mm^3 in NSG mice, respectively.

CAR T therapies and combination therapies

For the monotherapy with CAR T cells, CD45.1 mouse MigR control, Meso-CAR, or FAP-CAR T cells (generated as described above) were i.v. injected into tumor-bearing CD45.2 C57BL/6 mice at dose of 5 × 10^6 CAR^+ T cells/mouse; PBS was used as control. Tumor tissue was collected at 1- and 2-weeks post T cells administration. For the survival analysis, mice were euthanized when tumor volume reached ~2000 mm^3.

For the therapeutic combination of CAR T cells with anti-PD-1, CD45.1 mouse MigR control or FAP-CAR T cells were generated and i.v. injected into tumor-bearing CD45.2 C57BL/6 mice at dose of 5 × 10^6 CAR^+ T cells/mouse when the tumor volume reached 100-150 mm^3. Isotype control or anti-PD-1 (5 mg/kg twice a week) were i.p. injected into tumor-bearing mice 4 days post T cells administration. Tumor tissues were collected at day 17 post T cells administration for analysis. For the mice survival analysis, mice were euthanized when tumor volume reached ~2000 mm^3.

For the dual doses of CAR T cell therapy, CD45.1 mouse MigR control, Meso-CAR or FAP-CAR T cells were generated and i.v. injected into tumor-bearing CD45.2 C57BL/6 mice or NSG mice at dose of 5 × 10^6 CAR^+ T cells/mouse. 2 weeks later, the tumor-bearing mice treated with MigR control T cells were given again with MigR control T cells at dose of 5 × 10^6 GFP^+ T cells/mouse. Those treated with Meso-CAR T cells were

treated with either MigR control or Meso-CAR T cells at dose of 5×10^6 CAR^+ T cells/mouse. The mice treated with FAP-CAR T cells were then given either MigR control, FAP-CAR, or Meso-CAR T cells at dose of 5×10^6 CAR^+ T cells/mouse. Tumor tissues were collected 31 days post T cells administration for analysis. For the mice survival analysis, mice were euthanized when tumor volume reached ~3200 mm^3 in C57BL/6 mice or 800 mm^3 in NSG mice.

CAR T cells treatment in autochthonous KPC mice

Fully backcrossed C57BL/6 KPC mice were monitored by ultrasound (Vevo 2100 Micro-Ultrasound, Visual Sonics) and randomly assigned for treatment. 5×10^6 CAR^+ MigR control, Meso-CAR or FAP-CAR T cells were i.v. injected into these mice when they had established pancreatic tumors of 50-100 mm^3. Tumor tissue was collected at 1- and 2-weeks post T cells administration. For the dual dose of CAR T cell therapies, 5×10^6 CAR^+ MigR control, Meso-CAR or FAP-CAR T cells were i.v. injected into established KPC mice. 2 weeks later, the mice treated with either MigR control or Meso-CAR T cells were given second dose of Meso-CAR T cells, while the mice treated with FAP-CAR T cells were given a second dose of FAP-CAR T cell or Meso-CAR T cells (5×10^6 CAR^+ T cells/mouse). For the survival analysis, mice were euthanized when tumor volume reached ~1000 mm^3.

Multiparametric flow cytometry of tumors, spleen, and peripheral blood cells

Tumor tissue was dissected and digested with 2.5 mg/mL Collagenase type 2 (Worthington) plus 0.25 mg/mL DNase I (Roche) in RPMI-1640 for 30 minutes with intermittent shaking at 37°C. Digestion mixture was passed through 70 µm followed by 40 µm cell strainers (FALCON) to prepare single cell suspension and washed with stain buffer (BD Biosciences). The spleens were mashed and passed through 40 µm cell

strainer (FALCON). Red blood cells (RBC) were removed using RBC lysis buffer (BD Biosciences). Blood was collected through retro-orbital bleeding and RBC was removed using the same RBC lysis buffer. After washing with PBS, cells were collected.

Live/Dead Fixable Aqua Dead Cell Stain Kit (Invitrogen) was stained for 20 minutes on ice to exclude dead cells. Single cells were blocked with anti-mouse CD16/CD32 (Invitrogen) for 15 minutes followed by cell surface staining with antibodies diluted in stain buffer (BD Biosciences) for 30 min on ice. For detecting intracellular cytokine, single cell suspensions were incubated for 5 hours with Cell Activation Cocktail (BioLegend) which is a pre-mixed cocktail with optimized concentration of PMA (phorbol 12-myristate-13-acetate), ionomycin, and protein transport inhibitor (Brefeldin A) at 37°C. Intracellular staining for GzmB, IFN-γ, TNF-α, mesothelin, CD206 and TGF-β was performed with the use of Fixation/Permeabilization Solution Kit (BD Biosciences), while Ki-67 and FoxP3 staining were performed with Foxp3/Transcription Factor staining buffer set (eBiosciences) according to the manufacturer's instructions. Antibodies used in flow analysis are described in the KEY RESOURCES TABLE. Flow cytometric analysis was performed on a Symphony A3 or LSR Fortessa flow cytometer (BD Biosciences) and analyzed using FlowJo software (FlowJo LLC, USA).

Multiplex immunofluorescence staining

Tumors removed from mice using forceps were fixed in Prefer fixation buffer (ANATECH) overnight at room temperature. Prefer-fixed paraffin-embedded (PFPE) sections were cut at 5 mm thickness, deparaffinized and rehydrated. Epitope retrieval was performed using citrate buffer (Sigma-Aldrich) using a pressure cooker (Bio SB) at low pressure (106-110°C) for 5 min. PFPE sections were washed with PBS, incubated with blocking buffer (3%BSA with 0.3%Triton X-100 in PBS) for 1 hour at room temperature, and then stained with primary antibodies in blocking buffer at 4°C overnight. Samples were

stained with the following antibodies: FAP (1:250, Abcam), PDGFRα (1:200, R&D System), PDPN (1:200, R&D System), FITC-αSMA (1:500, Sigma), AF647-EpCAM (1:100, BioLegend), GFP (1:500, Abcam), CD3 (1:100, Abcam), CD8 (1:500, Abcam), CD4 (1:500, Abcam), FoxP3 (1:100, Abcam), F4/80 (1:100, Abcam), CD103 (1:100, Abcam), Ly6C+Ly6G (1:100, Abcam), CK19 (1:100, Abcam), Ki-67 (1:100, Abcam), CD31 (1:200, R&D System), IFN-γ (1:100, R&D System), TGF-β1 (1:100, Bioss), AF488 Pan-CK (1:100, eBiosciences), CD206 (1:100, R&D System), PD-1 (1:100, R&D System), biotin CHP (1:10, 3Helix), FN (1:300, Sigma-Aldrich), and cleaved caspase-3 (1:100, Cell Signaling Technology). Slides were then blocked again for 1 h and incubated with secondary antibodies in blocking buffer for 1 h, except for some that need to perform with tyramide signaling amplification (TSA) staining (Invitrogen). All primary, secondary antibodies and TSA kits used in multiplex IF staining are described in the KEY RESOURCES TABLE. Slides were washed with PBS for once, incubated with DAPI for 5 min, then washed 3 times with PBS and mounted with ProLong™ Diamond Antifade Mountant (with DAPI, Invitrogen). The whole sections with multiplex IF staining were scanned by Nikon Ti-E inverted microscope (Nikon). NIS-Elements Advanced Research software (Nikon, version 4.50) was used to process the images and FIJI-ImageJ was used to analyze the images.

Real-time fragment-based two-photon microscopy

Tumor slices were prepared as described previously[30], with modifications. In brief, tumors were embedded in 5% low-gelling-temperature agarose (Sigma-Aldrich) prepared in PBS. Tumors were cut with a vibratome (Leica VT1200S vibratome) in a bath of ice-cold PBS. The thickness of the slices was 500 μm. Live tumor slices were stained with AF647-anti-mouse CD90.2 (BioLegend) at a concentration of 10 μg/mL for 15 minutes at 37°C and were then transferred to 0.4-mm organotypic culture inserts

(Millipore) in 35-mm Petri dishes containing 1 mL RPMI-1640 (without phenol red; ThermoFisher) before imaging.

Imaging fresh slices of mouse tumors was performed using Leica SP8-MP upright multiphoton microscope with Coherent Chameleon Vision II MP laser equipped with a 37°C thermostatic chamber. Tumor slices were secured with a stainless-steel ring slice anchor (Warner Instruments) and perfused at a rate of 0.3 mL/min with a solution of RPMI (without phenol red), bubbled with 95% O_2 and 5% CO_2. Images were systematically acquired at 6 different regions within the tumor with a 20× (1.0 NA) water immersion lens and a Coherent Chameleon laser at 880 nm/25 mW. The following filters were used for fluorescence detection: CFP (483/32), GFP (535/30), AF647 (685/40) and tdTomato (610/75). For four-dimensional analysis of cell migration, a 70-90 µm z-stack at 5 µm step size was acquired for 2 hours, alternating between six fields every 30 seconds. Videos were made by compressing the z information into a single plane with the max intensity z projection of Imaris and LAS X software.

Image analysis was performed at PennVet Imaging Core (University of Pennsylvania). A 3D image analysis was performed on x, y, and z planes using Imaris 7.4 software. First, superficial planes from the top of the slice to 15 µm in depth were removed to exclude T cells located near the cut surface. Cellular motility parameters were then calculated using Imaris. Tracks >10% of the total recording time were included in the analysis. When a drift in the x, y dimension was noticed, it was corrected using the “Correct 3D Drift” plug-in in FIJI-ImageJ. CAR T cell number and motility were quantified in different tumor regions, including stroma-rich and tumor-nest regions. These regions were identified by visual inspection of immunofluorescence images. Stroma-rich region was defined by high CD90.2$^+$ area with a clear border between stromal cells and mCerulean$^+$ tumor cells. Tumor-rich region was defined by high Cerulean$^+$ area and

stromal cells were interlaced with Cerulean^{+} tumor cells. Fluorescence intensities were determined in regions of interest using FIJI-ImageJ. The number of T cells in defined regions was quantified using the Analyze Particles function of FIJI-ImageJ from fluorescent images that were first thresholded and then converted to binary images. Collagen measurement was performed using CT-FIRE software (version 2.0 beta) (https://loci.wisc.edu/software/ctfire)[55].

QUANTIFICATION AND STATISTICAL ANALYSIS

All experiments described here are the representative of at least three independent experiments (n ≥ 5 mice for each group unless specifically indicated). For *in vitro* experiments, cells, or tissues from each of these animals were processed (at least) in biological triplicates. All data here were shown as average ± S.D. or average ± S.E.M. Statistical analysis between two groups was conducted with a 2-tailed Student t test. multiple comparisons were performed by using one-way ANOVA or two-way ANOVA analysis with Tukey's multiple-comparison. Tumor growth curve analysis was conducted with Repeated-measure two-way ANOVA (mixed-model) with Tukey's multiple-comparison. Kaplan-Meier curves were used to analyze the survival data, and Cox regression was used to compute hazard ratio. No methods were used to determine whether the data met assumptions of the statistical approach. All statistical analysis was performed using GraphPad Prism 9 and the results of statistical analyses for each experiment are clearly indicated in the respective figures and in Figure Legends. p values <0.05 were considered significant.

Resource availability

Lead contact

Further information and requests for resources and reagents should be directed to and will be fulfilled by the lead contact, Dr. Ellen Puré (epure@upenn.edu).

Materials availability statement

Mouse lines and constructs generated in this study can be requested from the lead contact and obtained under appropriate MTA or/and license from the University of Pennsylvania.

Data and code availability

No original code was generated related to any of the data in this study.

Any additional information required to analyze the data reported in this study is available from the lead contact upon appropriate request.

Acknowledgements and funding:

This work was supported by sponsored research agreements from TMUNITY Therapeutics to E.P and S.M.A, NIH/NCI P01 CA217805 to S.M.A. and E.P., and CRI Irvington fellowship (Grant #: CRI4168) from Cancer research institute to Z.X.

Author contributions

E.P. and Z.X. conceived the project and designed the experiments. Z.X., M.K., and L.H. conducted the experiments and acquired the data. Z.X. generated CAR T cells, performed tumor killing assays and slice-based real-time two-photon microscopy. Z.W. and W.G. generated the mesothelin knockout line. Z.X., Z.L., L.H., and M.K. performed the mouse experiments. L.T., J.S., and E.P. designed and prepared the plasmids. Z.X., and Y.L. performed pathological analyses. Z.X. and L.H. performed the statistical analysis, analyzed, and interpreted the data. Z.X. and E.P. wrote the manuscript. E.P.,

C.H.J., and S.M.A provided guidance on experiments and edited the paper. All authors have read and approved the final manuscript.

DECLARATION OF INTERESTS

C.H.J., S.M.A., and E.P. are scientific founders and hold equity in Capstan Therapeutics. S.M.A. is on the scientific advisory boards of Verismo and Bioardis. C.H.J. is a scientific founder and has equity in Tmunity Therapeutics and DeCART Therapeutics, reports grants from Tmunity Therapeutics, and is on the scientific advisory boards of BluesphereBio, Cabaletta, Carisma, Cellares, Celldex, ImmuneSensor, Poseida, Verismo, Viracta Therapeutics, WIRB Copernicus Group, and Ziopharm Oncology. S.M.A., E.P., L.T. and J.S. are inventors (University of Pennsylvania) on a patent (10329355) and patent application for the 4G5 FAP CAR (Patent Applications 20210087294 and 20210087295). S.M.A., and E.P. are inventors (University of Pennsylvania) on a patent for the use of CAR T therapy in heart disease (US Provisional Patent Application 62/563,323 filed 26 September 2017, WIPO Patent Application PCT/US2018/052605). In accordance with the University of Pennsylvania policies and procedures and our ethical obligations as researchers, C.H.J. is named on additional patents that describe the creation and therapeutic use of chimeric antigen receptors. These interests have been fully disclosed to the University of Pennsylvania, and approved plans are in place for managing any potential conflicts arising from licensing these patents.

References

1. Hou, A.J., Chen, L.C. & Chen, Y.Y. Navigating CAR-T cells through the solid-tumour microenvironment. *Nature reviews. Drug discovery* **20**, 531-550 (2021).
2. Balkwill, F.R., Capasso, M. & Hagemann, T. The tumor microenvironment at a glance. *Journal of cell science* **125**, 5591-5596 (2012).

3. Darvin, P., Toor, S.M., Sasidharan Nair, V. & Elkord, E. Immune checkpoint inhibitors: recent progress and potential biomarkers. *Experimental & molecular medicine* **50**, 1-11 (2018).
4. Ullman, N.A., Burchard, P.R., Dunne, R.F. & Linehan, D.C. Immunologic Strategies in Pancreatic Cancer: Making Cold Tumors Hot. *Journal of clinical oncology : official journal of the American Society of Clinical Oncology* **40**, 2789-2805 (2022).
5. Srivastava, S. & Riddell, S.R. Chimeric Antigen Receptor T Cell Therapy: Challenges to Bench-to-Bedside Efficacy. *J Immunol* **200**, 459-468 (2018).
6. Galluzzi, L., Chan, T.A., Kroemer, G., Wolchok, J.D. & Lopez-Soto, A. The hallmarks of successful anticancer immunotherapy. *Science translational medicine* **10** (2018).
7. Kammertoens, T., Schuler, T. & Blankenstein, T. Immunotherapy: target the stroma to hit the tumor. *Trends Mol Med* **11**, 225-231 (2005).
8. Feig, C. *et al.* Targeting CXCL12 from FAP-expressing carcinoma-associated fibroblasts synergizes with anti-PD-L1 immunotherapy in pancreatic cancer. *Proceedings of the National Academy of Sciences of the United States of America* **110**, 20212-20217 (2013).
9. Lo, A. *et al.* Tumor-Promoting Desmoplasia Is Disrupted by Depleting FAP-Expressing Stromal Cells. *Cancer research* **75**, 2800-2810 (2015).
10. Neesse, A. *et al.* Stromal biology and therapy in pancreatic cancer. *Gut* **60**, 861-868 (2011).
11. Wang, L.C. *et al.* Targeting fibroblast activation protein in tumor stroma with chimeric antigen receptor T cells can inhibit tumor growth and augment host immunity without severe toxicity. *Cancer immunology research* **2**, 154-166 (2014).
12. Winograd, R. *et al.* Induction of T-cell Immunity Overcomes Complete Resistance to PD-1 and CTLA-4 Blockade and Improves Survival in Pancreatic Carcinoma. *Cancer immunology research* **3**, 399-411 (2015).
13. Chen, Y., McAndrews, K.M. & Kalluri, R. Clinical and therapeutic relevance of cancer-associated fibroblasts. *Nature reviews. Clinical oncology* **18**, 792-804 (2021).
14. Whittle, M.C. & Hingorani, S.R. Fibroblasts in Pancreatic Ductal Adenocarcinoma: Biological Mechanisms and Therapeutic Targets. *Gastroenterology* **156**, 2085-2096 (2019).
15. McAndrews, K.M. *et al.* Identification of Functional Heterogeneity of Carcinoma-Associated Fibroblasts with Distinct IL6-Mediated Therapy Resistance in Pancreatic Cancer. *Cancer Discov* **12**, 1580-1597 (2022).
16. Kakarla, S. *et al.* Antitumor effects of chimeric receptor engineered human T cells directed to tumor stroma. *Molecular therapy : the journal of the American Society of Gene Therapy* **21**, 1611-1620 (2013).
17. Grout, J.A. *et al.* Spatial Positioning and Matrix Programs of Cancer-Associated Fibroblasts Promote T-cell Exclusion in Human Lung Tumors. *Cancer Discov* **12**, 2606-2625 (2022).
18. Qian, Y. *et al.* Molecular alterations and targeted therapy in pancreatic ductal adenocarcinoma. *Journal of hematology & oncology* **13**, 130 (2020).
19. Fan, J.Q. *et al.* Current advances and outlooks in immunotherapy for pancreatic ductal adenocarcinoma. *Mol Cancer* **19**, 32 (2020).
20. Barrett, R.L. & Puré, E. Cancer-associated fibroblasts and their influence on tumor immunity and immunotherapy. *eLife* **9** (2020).

21. Rahib, L. *et al.* Projecting cancer incidence and deaths to 2030: the unexpected burden of thyroid, liver, and pancreas cancers in the United States. *Cancer research* **74**, 2913-2921 (2014).
22. Espinet, E., Klein, L., Puré, E. & Singh, S.K. Mechanisms of PDAC subtype heterogeneity and therapy response. *Trends Cancer* **8**, 1060-1071 (2022).
23. Hegde, P.S. & Chen, D.S. Top 10 Challenges in Cancer Immunotherapy. *Immunity* **52**, 17-35 (2020).
24. Watanabe, K. *et al.* Pancreatic cancer therapy with combined mesothelin-redirected chimeric antigen receptor T cells and cytokine-armed oncolytic adenoviruses. *JCI Insight* **3** (2018).
25. Salmon, H. *et al.* Matrix architecture defines the preferential localization and migration of T cells into the stroma of human lung tumors. *The Journal of clinical investigation* **122**, 899-910 (2012).
26. Good, C.R. *et al.* An NK-like CAR T cell transition in CAR T cell dysfunction. *Cell* **184**, 6081-6100 e6026 (2021).
27. Lee, I.K. *et al.* Monitoring Therapeutic Response to Anti-Fibroblast Activation Protein (FAP) CAR T Cells using [18F]AlF-FAPI-74. *Clinical cancer research : an official journal of the American Association for Cancer Research* (2022).
28. Hingorani, S.R. *et al.* Trp53R172H and KrasG12D cooperate to promote chromosomal instability and widely metastatic pancreatic ductal adenocarcinoma in mice. *Cancer cell* **7**, 469-483 (2005).
29. Kleeman, B. *et al.* A guide to choosing fluorescent protein combinations for flow cytometric analysis based on spectral overlap. *Cytometry. Part A : the journal of the International Society for Analytical Cytology* **93**, 556-562 (2018).
30. Peranzoni, E. *et al.* Ex Vivo Imaging of Resident CD8 T Lymphocytes in Human Lung Tumor Slices Using Confocal Microscopy. *Journal of visualized experiments : JoVE* (2017).
31. Nicolas-Boluda, A. *et al.* Tumor stiffening reversion through collagen crosslinking inhibition improves T cell migration and anti-PD-1 treatment. *eLife* **10** (2021).
32. Kantari-Mimoun, C. *et al.* CAR T-cell Entry into Tumor Islets Is a Two-Step Process Dependent on IFNγ and ICAM-1. *Cancer immunology research* **9**, 1425-1438 (2021).
33. Morello, A., Sadelain, M. & Adusumilli, P.S. Mesothelin-Targeted CARs: Driving T Cells to Solid Tumors. *Cancer Discov* **6**, 133-146 (2016).
34. Verginadis, II *et al.* A stromal Integrated Stress Response activates perivascular cancer-associated fibroblasts to drive angiogenesis and tumour progression. *Nat Cell Biol* **24**, 940-953 (2022).
35. Helms, E., Onate, M.K. & Sherman, M.H. Fibroblast Heterogeneity in the Pancreatic Tumor Microenvironment. *Cancer Discov* **10**, 648-656 (2020).
36. Garcia, P.E. *et al.* Differential Contribution of Pancreatic Fibroblast Subsets to the Pancreatic Cancer Stroma. *Cellular and molecular gastroenterology and hepatology* **10**, 581-599 (2020).
37. Elyada, E. *et al.* Cross-Species Single-Cell Analysis of Pancreatic Ductal Adenocarcinoma Reveals Antigen-Presenting Cancer-Associated Fibroblasts. *Cancer Discov* **9**, 1102-1123 (2019).
38. Sahai, E. *et al.* A framework for advancing our understanding of cancer-associated fibroblasts. *Nat Rev Cancer* **20**, 174-186 (2020).
39. Lo, A. *et al.* Fibroblast activation protein augments progression and metastasis of pancreatic ductal adenocarcinoma. *JCI Insight* **2** (2017).
40. Derynck, R., Turley, S.J. & Akhurst, R.J. TGFβ biology in cancer progression and immunotherapy. *Nature reviews. Clinical oncology* **18**, 9-34 (2021).

41. Puré, E. & Hingorani, S.R. Mesenchymal Cell Plasticity and Perfidy in Epithelial Malignancy. *Trends Cancer* **4**, 273-277 (2018).
42. Paszek, M.J. *et al.* Tensional homeostasis and the malignant phenotype. *Cancer cell* **8**, 241-254 (2005).
43. Avery, D. *et al.* Extracellular matrix directs phenotypic heterogeneity of activated fibroblasts. *Matrix Biol* **67**, 90-106 (2018).
44. Calvo, F. *et al.* Mechanotransduction and YAP-dependent matrix remodelling is required for the generation and maintenance of cancer-associated fibroblasts. *Nat Cell Biol* **15**, 637-646 (2013).
45. David, C.J. *et al.* TGF-β Tumor Suppression through a Lethal EMT. *Cell* **164**, 1015-1030 (2016).
46. Peng, D., Fu, M., Wang, M., Wei, Y. & Wei, X. Targeting TGF-β signal transduction for fibrosis and cancer therapy. *Mol Cancer* **21**, 104 (2022).
47. Turley, S.J., Cremasco, V. & Astarita, J.L. Immunological hallmarks of stromal cells in the tumour microenvironment. *Nature reviews. Immunology* **15**, 669-682 (2015).
48. Mhaidly, R. & Mechta-Grigoriou, F. Role of cancer-associated fibroblast subpopulations in immune infiltration, as a new means of treatment in cancer. *Immunological reviews* **302**, 259-272 (2021).
49. Affo, S. *et al.* Promotion of cholangiocarcinoma growth by diverse cancer-associated fibroblast subpopulations. *Cancer cell* **39**, 866-882.e811 (2021).
50. Lau, E.Y. *et al.* Cancer-Associated Fibroblasts Regulate Tumor-Initiating Cell Plasticity in Hepatocellular Carcinoma through c-Met/FRA1/HEY1 Signaling. *Cell Rep* **15**, 1175-1189 (2016).
51. Srivastava, S. *et al.* Immunogenic Chemotherapy Enhances Recruitment of CAR-T Cells to Lung Tumors and Improves Antitumor Efficacy when Combined with Checkpoint Blockade. *Cancer cell* **39**, 193-208.e110 (2021).
52. Zhang, W. *et al.* ICAM-1-mediated adhesion is a prerequisite for exosome-induced T cell suppression. *Developmental cell* **57**, 329-343.e327 (2022).
53. Klampatsa, A. *et al.* Analysis and Augmentation of the Immunologic Bystander Effects of CAR T Cell Therapy in a Syngeneic Mouse Cancer Model. *Mol Ther Oncolytics* **18**, 360-371 (2020).
54. Aghajanian, H. *et al.* Targeting cardiac fibrosis with engineered T cells. *Nature* **573**, 430-433 (2019).
55. Bredfeldt, J.S. *et al.* Computational segmentation of collagen fibers from second-harmonic generation images of breast cancer. *Journal of biomedical optics* **19**, 16007 (2014).

Figure legends

Fig. 1: Stromal-targeted FAP-CAR T cells inhibit PDAC tumor growth more effectively than Meso-CAR T cells. (a) Depiction of control MigR, Meso-CAR and FAP-CAR recombinant MigR constructs. **(b-d) Comparable transduction efficiency, CAR expression and function of FAP- and Meso-CAR T cells *in vitro*. (b)** Flow cytometric

analysis of EGFP expression (Y-axis) and reactivity with CAR binding APC-conjugated anti-F(ab')$_2$ fragment antibodies (X-axis) demonstrated comparable transduction efficiency for all three constructs compared to untransduced (UTD) control T cells. FAP-CAR T cells and Meso-CAR T cells exhibit comparable **(c)** cytotoxic activity and **(d)** IFN-γ release when cultured with target cells expressing their specific targets, Meso$^+$ 4662 tumor cells and murine FAP transfected 3T3 cells, relative to negative control Meso-KO 4662 cells and FAP-negative parental 3T3 cells, respectively. Percent specific cell lyses was determined using MTS (Meso) or luciferase (FAP) assay performed in triplicate and presented as mean ± SD. The levels of IFN-γ accumulated in the conditioned media from the killing assay was determined by ELISA. Data points are mean ± SD and groups were compared using two-way ANOVA with Tukey's multiple comparisons test. ****$p < 0.0001$. **(e-k) Impact of FAP-CAR T vs. Meso-CAR T on growth of (e-i) established 4662 tumors subcutaneously transplanted into syngeneic mice and (j-k) established spontaneous pancreatic tumors in KPC mice. (e)** Experimental timeline for treatment of 4662 syngeneic PDAC tumor bearing C57BL/6 mice. Average **(f)** and individual **(g)** growth curves, tumor weight at endpoint **(h)** and modified Kaplan-Meier curves **(i)** for each treatment cohort in the syngeneic transplant model. Average tumor growth curves measured by ultrasound **(j)** and modified Kaplan-Meier plots **(k)** for spontaneous tumors in KPC mice for each indicated treatment cohort. Data indicate mean ± SD (n = 5 per group) and were determined by one-way ANOVA with Tukey's multiple comparisons test **(F, H, and J)** or log-rank test **(I and K)**. *$p < 0.05$, **$p < 0.01$, ***$p < 0.001$, and ****$p < 0.0001$.

Fig. 2: FAP-CAR T cells infiltrate and deplete their target cells more effectively than Meso-CART cells in PDAC tumors. (a) Schematic of experimental protocol: 4662 tumor cells were injected subcutaneously into syngeneic CD45.2 C57BL/6 mice. When

tumors reached 100-150 mm^3, the mice were injected i.v. with 5×10^6 MigR control, Meso-CAR$^+$ T or FAP-CAR$^+$ T cells generated using T cells isolated from CD45.1 C57BL/6 donor mice. Flow cytometry, multiplex IF, and two-photon microscopy were performed on 5 mice per group at 1, 4 and 7 days post-adoptive T cell transfer. **(b)** Representative flow cytometry plots of tumor-infiltrating MigR control, Meso-CAR, and FAP-CAR T cells are depicted on the left. The adjacent bar graphs on the right depict the average ± SD of the number of CD45.1$^+$GFP$^+$ CAR T cells recovered per 0.2 grams of tumor tissue (top) and the percent of CD45.1$^+$GFP$^+$ CAR T cells amongst total live cells recovered (bottom) at each time point for each group. Flow cytometry was used to determine expression of PD-1 **(c)**, Ki-67 **(d)** and IFN-γ **(e)** the tumor-infiltrating MigR control, Meso-CAR and FAP-CAR T cells at day 7 post-administration. For each analysis, representative flow plots are shown on the left and quantification of the average ± SD for each cohort to the right. **(f)** Quantification of flow cytometric analysis demonstrating time-dependent decrease in FAP$^+$ cells (top), and Pearson correlation analysis indicating that reduction of FAP$^+$ cells in individual mice in the FAP-CAR treated cohort correlated with the extent of FAP-CAR T cell infiltration of tumors (middle). Reduction in mesothelin$^+$ cell recovery was modest and only evident by day 7 post-Meso-CAR T cell administration (bottom). **(g)** Representative multiplex IF images (left) showing the localization of CAR T cells and their spatial relationships to FAP$^+$ stromal cells and EpCAM$^+$ tumor cells in syngenetic transplanted 4622 tumors. Quantification of the IF images from all mice is depicted in the adjacent bar graphs (right). **(h)** Representative multiplex IF images (left) showing the localization of CAR T cells and their spatial relationships to FAP$^+$ stromal cells and PanCK$^+$ tumor cells in spontaneous pancreatic tumors in KPC mice. Quantification of the IF images from all mice is depicted in the adjacent bar graphs (right). Data points are mean ± SD (n = 5 per group) and groups were compared using one-way ANOVA analysis with Dunnett's multiple comparison tests **(c, d, e, h)** or two-

way ANOVA with Tukey's multiple comparisons tests **(b, f, g)**. *p < 0.05, **p < 0.01, ***p < 0.001, and ****p < 0.0001.

Fig. 3: FAP-CAR T cells overcome the physical barrier and immunosuppressive TME to infiltrate tumor nests. (a) Workflow for the slice-based real-time two-photon microscopy with systematic imaging. **(b)** Representative static images from two-photon microscopy at different subregions in the tumors treated with MigR control, Meso-CAR, or FAP-CAR T cells at indicated timepoints. The GFP^+ (green) T cells are indicated by red arrows. $CD90.2^+$ stromal cells in magenta, $mCerulean^+$ tumor cells in cyan, and SHG for fibrillar collagen in gray. Scale bar, 100 µm. **(c)** Quantification of GFP^+ T cells, $CD90.2^+$ stromal cells, SHG fiber number, and SHG^+ area in stroma-rich regions (left column) and tumor nests (right column) at day 1, 4 and 7 post-administration. **(d)** Quantification of parameters of T cell motility for GFP^+ MigR control (black symbols), Meso-CAR (blue symbols), and FAP-CAR (red symbols) T cells, including mean track speed (left), track length (middle), and track straightness (right), at day 7 post-administration using Imaris software. **(e)** Quantification of GFP^+ FAP-CAR T cell mobility in stroma-rich (top) and tumor nest (bottom) regions, including mean track speed (left), track length (middle), and track straightness (right), at days 1, 4 and 7 post-FAP-CAR T cells administration. Data points represent individual cell measurements, and the bars represent mean ± SD (n = 5); groups were compared using two-way ANOVA with Tukey's multiple comparisons tests **(c)** or one-way ANOVA analysis with Dunnett's multiple comparison tests **(d and e)**. *p < 0.05, **p < 0.01, ***p < 0.001, and ****p < 0.0001.

Fig. 4: Ablation of FAP^+ cells alters the stromal landscape, rapidly depletes matrix and enhances T cell infiltration. (a) Representative (top) and quantification of (bottom) multiplex immunofluorescence images in tumors 1 week (left) and 2 weeks (right) post-

treatment with PBS, MigR control or FAP-CAR T cells. First row depicts staining for stromal cell profiles, including FAP (green), α-SMA (red) and PDGFR-α (magenta). Second row depicts staining for ECM components including collagen hybridizing peptide (CHP) that detects remodeled collagen (red) and FN (green). Third row depicts distribution of T cells (CD3, red) and their spatial relationships to tumor cells (PanCK, green) and stromal cells (PDPN, magenta). Nuclei were stained with DAPI (blue). Scale bar: 100 μm. **(b)** t-SNE of multi-parametric flow cytometry demonstrating the immune cell profiles, including lymphocyte (left) and myeloid cells (right) in tumors 1 week (Top row) and 2 weeks (bottom row) post-treatment with PBS, MigR control or FAP-CAR T cells. The percentages of indicated immune cell subpopulations in total live cells or CD45.2$^+$ cells from tumors for each group of mice quantified based on multi-parametric flow cytometry analysis. Data points are mean ± SD (n = 5) and groups were compared using two-way ANOVA with Tukey's multiple comparisons tests. *$p < 0.05$, **$p < 0.01$, ***$p < 0.001$, and ****$p < 0.0001$.

Fig. 5: Ablation of FAP$^+$ cells by FAP-CAR T cells enhances the efficacy of anti-PD-1 antibody immune checkpoint therapy. (a) Treatment protocol: 4662 tumor-bearing CD45.2 C57BL/6 mice were treated with MigR control or FAP-CAR T cells followed by isotype or anti-PD-1 antibodies. **(b)** Average tumor growth curves in mice in indicated treatment groups. **(c)** Individual tumor growth curves for mice in each of the indicated treatment groups. **(d)** End-point tumor weights in indicated treatment groups. **(e)** Modified Kaplan-Meier curve for mice in indicated treatment groups. **(f)** Quantification of tumor-infiltrating MigR control or FAP-CAR T cells expressing both CD45.1 and EGFP, FAP$^+$ cells and PD-1 expression in endogenous CD8$^+$ T cells in tumors at end-point. **(g)** Representative multiplex IF images of FAP (green) and α-SMA (red) (top row, as well as CD8 (green) and PD-1 (red) (bottom row in end-point tumors for indicated treatment

groups. Nuclei were stained with DAPI (blue). Scale bar, 100 μm. **(h)** Quantification of FAP, α-SMA, CD8, and PD-1 in end-point tumors from mice from indicated treatment groups based on multiplexed IF analysis. **(i)** Quantification of tumor infiltrating endogenous $CD8^+$ T cells and total Tim-3^+, TNF-α^+, and IFN-γ^+ T cells upon re-stimulation *ex vivo* based on flow cytometry analysis. Data points are mean ± SD (n = 8) and groups were compared using one-way ANOVA analysis with Dunnett's multiple comparison tests **(b, d, f, h, and i)** or log-rank test **(e)**. *$p < 0.05$, **$p < 0.01$, ***$p < 0.001$, and ****$p < 0.0001$.

Fig. 6: Ablation of FAP^+-CAFs by FAP-CAR T cells enhances the efficacy of subsequent treatment with TAA Meso-CAR T cells in PDAC tumors. (a) Treatment protocol: C57BL/6 mice bearing established 4662 tumors were treated with the indicated first dose of T cells and 15 days later treated with the second dose of indicated T cells. **(b)** Average growth curves and **(c)** tumor weights of tumors at end-point for each of the indicated treatment groups. **(d)** Modified Kaplan-Meier curves of mice from each of the indicated treatment groups. **(e)** Treatment protocol: established KPC mice were treated with the indicated first dose of T cells and 15 days later treated with the second dose of indicated T cells. **(f)** Average growth curves and **(g)** modified Kaplan-Meier curves of KPC mice from each of the indicated treatment groups. **(h)** Treatment protocol: NSG mice bearing established AsPC-1 human PDAC tumors were treated with the indicated first dose of T cells and 15 days later treated with the second dose of indicated T cells. **(i)** Average growth curves and **(j)** modified Kaplan-Meier curves of AsPC-1 human PDAC bearing NSG mice from each of the indicated treatment groups. **(k)** Representative multiplexed IF images (top panels) and quantification (bottom panels) of sections of end-point tumors from each of the indicated treatment groups stained for cleaved caspase-3, Ki-67, TGF-β or CD31 (red) as indicated and in each case co-stained with Pan-CK

(green). Nuclei were stained with DAPI (blue). Scale bar, 100 µm. Data points are mean ± SD (n = 5) and groups were compared using one-way ANOVA analysis with Dunnett's multiple comparison tests **(b, c, f, i and k)** or log-rank test **(d, g and j)**. *p < 0.05, **p < 0.01, ***p < 0.001, and ****p < 0.0001.

Fig. 7: FAP-CAR T cells rendered tumors permissive to Meso-CAR T cells allowing their infiltration and function within tumor. (a) Treatment protocol: 4662 tumor-bearing CD45.1 C57BL/6 mice (hosts) were treated with donor CD45.2 GFP^+ MigR control, CD45.2 GFP^+ Meso-CAR or CD45.2 GFP^+ FAP-CAR T cells. 4 days later, all mice received a second treatment of CD45.2 $tdTomato^+$ Meso-CAR T cells. Tumors were collected for analysis at day 1, 4 and 7 post-second treatment and tumors analyzed by two-photon microscopy, flow cytometry and multiplexed IF. **(b)** Representative static images from two-photon microscopy at different subregions in the tumors treated with GFP^+ MigR control, GFP^+ Meso-CAR, or GFP^+ FAP-CAR T cells with subsequent $tdTomato^+$ Meso-CAR T cells at indicated time points. The GFP^+ T cells from first treatment appear green and $tdTomato^+$ Meso-CAR T cells from second treatment appear red and examples of latter are highlighted by white arrows. $CD90.2^+$ stromal cells appear magenta and $mCerulean^+$ tumor cells cyan. Scale bar, 100 µm. **(c)** Quantification of $tdTomato^+$ Meso-CAR T cells (Top panels) and $mCerulean^+$ tumor cells (bottom panels) in stroma-rich (left) and tumor nest (right) regions at day 1, 4 and 7 post administration. **(d)** Representative flow plots and quantification of flow cytometry analysis of $tdTomato^+$ Meso-CAR T cells in tumors from the indicated treatment groups at the indicated times post-second treatment. **(e)** Quantification of the expression of GzmB, IFN-γ and TNF-α by examined for the infiltrating $tdTomato^+$ Meso-CAR T cells in tumors from each of the indicated treatment groups at the indicated times post-second treatment. Data points are mean ± SD (n = 5) and groups were compared using two-way

ANOVA with Tukey's multiple comparisons tests **(c and d)** or one-way ANOVA analysis with Dunnett's multiple comparison tests **(e)**. *$p < 0.05$, **$p < 0.01$, ***$p < 0.001$, and ****$p < 0.0001$.

Fig. 8: Sequential administration of FAP-CAR T cells with Meso-CAR T cells enhances systemic endogenous adaptive anti-tumor immunity in PDAC models. (a) Treatment protocol: C57BL/6 mice bearing established 4662 tumors were treated with the indicated first dose of T cells and 15 days later treated with the second dose of indicated T cells. **(b-d)** Quantification of tumor infiltrating endogenous $CD8^+$ T cells and $CD4^+FoxP3^+$ Treg cells **(b)**, IFN-γ expression in tumor-infiltrating and splenic endogenous $CD8^+$ T cells upon restimulation *ex vivo* **(c)**, Ly-$6C^{low}$Ly-$6G^+$ myeloid cells, $CD11b^+F4/80^+$ macrophages, and $CD206^+F4/80^+$ macrophages **(d)** by flow cytometric analysis. **(e)** Representative flow plots and quantification of flow cytometry analysis of $CD103^+CD11c^+$ cDC1 cells in tumors from the indicated combination treatment groups. **(f)** Representative images (left panels) and quantification (right panels) of multiplexed immunofluorescence staining of sections of end-point tumors from each of the indicated treatment groups stained for CD8 (cyan) and IFN-γ (magenta), CD4 (cyan) and FoxP3 (magenta), F4/80 (cyan) and CD206 (magenta), Gr-1 (cyan) and CD103 (magenta) as indicated and in each case co-stained with EpCAM (yellow). Nuclei were stained with DAPI (blue). Scale bar, 100 μm. Data points are mean ± SD (n = 5) and groups were compared using one-way ANOVA analysis with Dunnett's multiple comparison tests **(b-f)**. *$p < 0.05$, **$p < 0.01$, ***$p < 0.001$, and ****$p < 0.0001$.

Extended Data Fig. 1 (Related to Fig. 1): Comparable proliferation and functionality of Meso-CAR and FAP-CAR T cells *in vitro*. (a) Histogram of mesothelin expression in parental 4662 and 4662 mesothelin KO cell line analyzed by flow cytometry. **(b)** Comparable proliferation of MigR, Meso-CAR T and FAP-CAR T cells induced by anti-CD3/28-beads *in vitro.* **(c)** Representative flow cytometry plots (left) and quantification (right) of CAR T cell expression of GzmB, TNF-α, and IFN-γ 2 days post-activation with anti-CD3/28 beads *in vitro*. **(d)** Migration of MigR, Meso-CAR-T and FAP-CAR T cells in dual chamber wells from upper chamber containing media to lower chamber containing CXCL9 (left) quantified (right). Data indicate mean ± SD (n = 3). Statistical analysis is performed using one-way ANOVA analysis with Dunnett's multiple comparison tests **(b, c and d)**.

Extended Data Fig. 2 (Related to Fig. 1): Stromal-targeted FAP-CAR T cells inhibited tumor growth more effectively than Meso-CAR T cells in syngeneic transplant models and autochthonous models of PDAC. (a) Average time-dependent fold change in tumor volume in subcutaneous PDAC transplant models with indicated treatments. **(b)** Tumor volume changes for individual transplanted 4662 tumors in syngeneic C57BL/6 mice relative to baseline (just prior to treatment indicated as 100% (brown dashed line) for each individual tumor. Growth above this line indicates tumor progression. The black dashed line indicates each tumor at a volume of 250% compared to baseline. **(c)** Representative ultrasound images of tumor volume measurement in spontaneous pancreatic tumors in KPC mice following treatment with the indicated CAR T cells. **(d)** Average time-dependent fold change in tumor volume in spontaneous pancreatic tumors in KPC mice following treatment with the indicated CAR T cells. **(e)** Individual tumor growth curves in KPC mice post treatments. **(f)** Tumor volume changes for individual spontaneous pancreatic tumors in KPC mice relative to baseline as

described in B. Data indicate mean ± SD (n = 10 for **a and b**, n = 5 for **d-f**) and were compared by one-way ANOVA with Tukey's multiple comparisons test **(a and d)**. *p < 0.05, **p < 0.01, ***p < 0.001, and ****p < 0.0001.

Extended Data Fig. 3 (Related to Fig. 2): FAP-CAR T cells and Meso-CART cells behave comparably in circulation. Quantification and characterization by flow cytometry of CAR T cell expression of CD69, Ki-67 and PD-1 in blood **(a)** and spleen **(b)**. Data indicate mean ± SD (n = 5). P values were determined by one-way ANOVA with Tukey's multiple comparisons test **(a and b)**. *p < 0.05, **p < 0.01, ***p < 0.001, and ****p < 0.0001.

Extended Data Fig. 4 (Related to Fig. 2): FAP-CAR T cells infiltrate and deplete their target cells more effectively than Meso-CART cells in PDAC tumors *in vivo*. (a) Gating strategy used to analyze flow cytometric data of tumor-infiltrating CAR T cells. **(b)** Representative flow cytometric images and **(c)** quantification of tumor-infiltrating CAR T expression of CD4 (top) and CD8 (bottom). Representative flow cytometric images of cells with expression of **(d)** FAP (stromal cells) or **(e)** mesothelin (tumor cells) in tumors following treatment with indicated T cells. Data indicate mean ± SD (n = 5). P values were determined by one-way ANOVA with Tukey's multiple comparisons test **(c)**. *p < 0.05, **p < 0.01, ***p < 0.001, and ****p < 0.0001.

Extended Data Fig. 5 (Related to Fig. 3): FAP-CAR T cells overcome the physical barrier and immunosuppressive TME to infiltrate tumor nests. (a) Mesothelin expression in mCerulean 4662 cell line was examined by flow cytometry. **(b-d)** Representative processing and quantification of SHG fiber number in the tumors at stroma-rich and tumor-nest regions at indicated time points post-T cell administration. **(e)** Representative static two-photon microscopy images of FAP-CAR T cells in the tumors at indicated time points post-administration, showing the extravasation and penetration

of peritumoral regions by FAP-CAR T cells. **(f)** A representative time-lapse image of FAP-CAR T cells (green) at 16 hours post-administration. The track of a T cell is shown by the white dotted line and white arrowheads at both ends of the track. *See Extended Data Movie 8*.

Extended Data Fig. 6 (Related to Fig. 6): Ablation of FAP$^+$ cells alters the stromal landscape, rapidly depletes matrix and enhances T cell infiltration. Gating strategies for profiling immune cells, including T cells, B cells, and myeloid cells depicted in Figure 4.

Extended Data Fig. 7 (Related to Fig. 6): Ablation of FAP$^+$-CAFs by FAP-CAR T cells enhances the efficacy of subsequent treatment with TAA Meso-CAR T cells in PDAC tumors. (a) Tumor growth curves of individual 4662 PDAC tumors transplanted into syngeneic mice following treatment with the indicated combination treatments. **(b)** Average fold change in tumor volume over time relative to baseline (just prior to first treatment) in each cohort administered the indicated combination treatments. **(c)** Tumor volume changes of individual 4662 PDAC tumors in mice receiving the indicated combination treatments. **(d)** Representative multiplex immunofluorescence images of tumors following indicated combination treatments. Top row, staining of FAP (green), α-SMA (red), PDGFR-α (magenta). Middle row, staining with CHP (red) and FN (green). Bottom row, staining of CD3 (red), Pan-CK (green) and PDPN (magenta). Nuclei were stained with DAPI (blue). Scale bar: 100 μm. **(e)** Quantification stromal cells (FAP, α-SMA, PDGFR-α, and PDPN), ECM (CHP and FN), tumor cells (PanCK) and total T cells (CD3) based on multiplexed immunofluorescence of end-point tumors from all mice in each cohort. **(f)** Quantification of TGF-β expression in different cell populations, including CD11b$^+$, FAP$^+$αSMA$^+$, FAP$^+$αSMA$^-$ and αSMA$^+$FAP$^-$ cells in dissociated end-point tumors from mice receiving indicated combination treatments.

Data indicate mean ± SD (n = 5). P values were determined by one-way ANOVA with Tukey's multiple comparisons test **(b, e and f)**. *p < 0.05, **p < 0.01, ***p < 0.001, and ****p < 0.0001.

Extended Data Fig. 8 (Related to Fig. 7): Disruption of tumor stroma by FAP-CAR T cells rendered tumors permissive to meso-CAR T cells allowing their infiltration and function within tumor. (a-b) Representative (top) and quantification (bottom) of flow cytometric analysis of **(a)** FAP^+ and **(b)** $mesothelin^+$ targeted cells in tumors post-treatment with indicated combinations. **(c)** Representative multiplex IF images showing CAR T cells from first treatment (GFP^+, green) and second treatment (expressing tdTomato, red) and expression of mesothelin (magenta). Nuclei were stained with DAPI (blue). Scale bar: 100 µm. **(e)** Quantifications of multiplexed immunofluorescence of GFP^+, $tdTomato^+$ and $mesothelin^+$ cells in all tumors from each treatment cohort. Data points are mean ± SD (n = 5) and groups were compared using two-way ANOVA with Tukey's multiple comparisons tests **(a, b and d)**. *p < 0.05, **p < 0.01, ***p < 0.001, and ****p < 0.0001.

Extended Data Fig. 9 (Related to Fig. 8): Sequential administration of FAP-CAR T cells with Meso-CAR T cells enhances systemic endogenous adaptive anti-tumor immunity in PDAC models. (a) Average growth curves of tumors at end-point for each of the indicated treatment groups. **(b-f)** Representative flow cytometric images (left panels) and quantification (right panels) of $CD8^+$ **(b)**, $CD4^+FoxP3^+$ **(c)**, $Ly\text{-}6C^+Ly\text{-}6G^+$ myeloid cells **(d)**, $CD11b^+F4/80^+$ macrophages **(e)**, and $F4/80^+CD206^+$ macrophages **(f)** in tumors at end-point with indicated combination treatments. Data points are mean ± SD (n = 5) and groups were compared using one-way ANOVA with Tukey's multiple comparisons test **(a-f)**. *p < 0.05, **p < 0.01, ***p < 0.001, and ****p < 0.0001.

Fig. 1

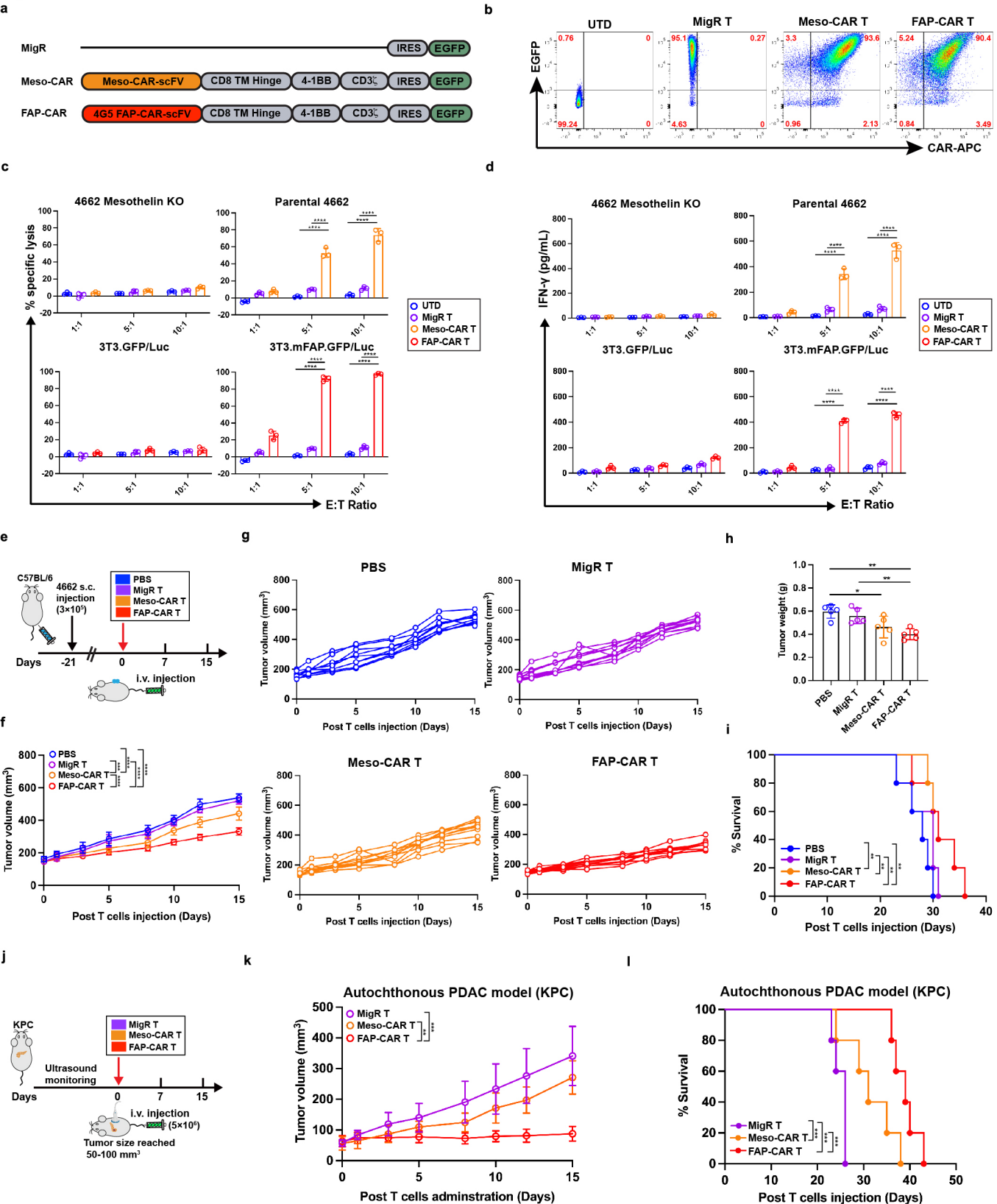
a
MigR
IRES
EGFP
Meso-CAR
Meso-CAR-scFV
CD8 TM Hinge
4-1BB
CD3ζ
FAP-CAR
4G5 FAP-CAR-scFV
b
UTD
MigR T
Meso-CAR T
FAP-CAR T
EGFP
CAR-APC
c
4662 Mesothelin KO
Parental 4662
3T3.GFP/Luc
3T3.mFAP.GFP/Luc
% specific lysis
E:T Ratio
d
IFN-γ (pg/mL)
e
C57BL/6
4662 s.c. injection (3×10⁵)
PBS
MigR T
Meso-CAR T
FAP-CAR T
Days
i.v. injection
f
Tumor volume (mm³)
Post T cells injection (Days)
g
PBS
MigR T
Meso-CAR T
FAP-CAR T
h
Tumor weight (g)
i
% Survival
j
KPC
Ultrasound monitoring
Tumor size reached 50-100 mm³
(5×10⁶)
k
Autochthonous PDAC model (KPC)
Post T cells adminstration (Days)
l

Fig. 2

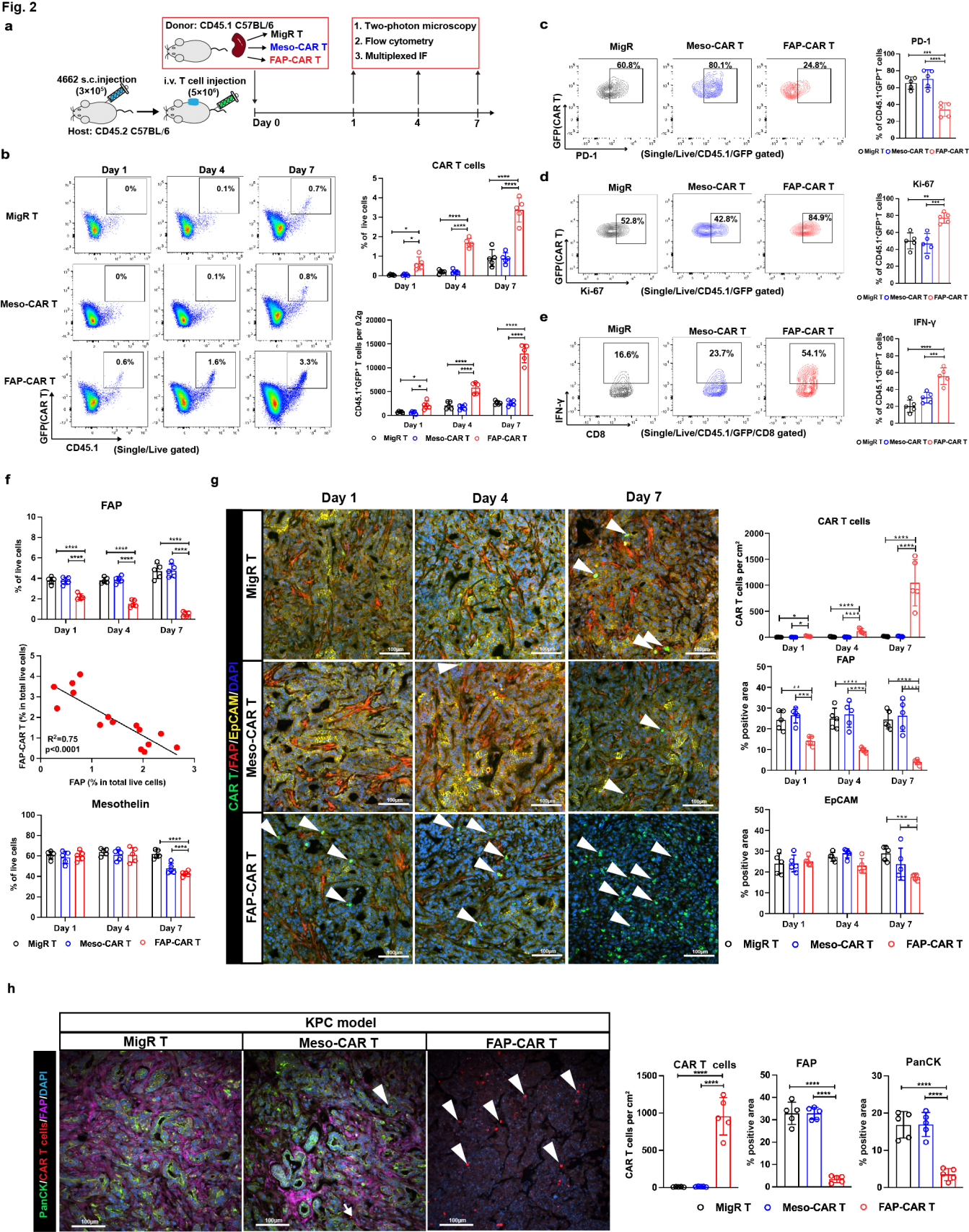
a
Donor: CD45.1 C57BL/6
MigR T
Meso-CAR T
FAP-CAR T
1. Two-photon microscopy
2. Flow cytometry
3. Multiplexed IF
4662 s.c.injection (3×10^5)
i.v. T cell injection (5×10^6)
Host: CD45.2 C57BL/6
Day 0
1
4
7
b
Day 1
Day 4
Day 7
MigR T
Meso-CAR T
FAP-CAR T
0%
0.1%
0.7%
0%
0.1%
0.8%
0.6%
1.6%
3.3%
GFP(CAR T)
CD45.1
(Single/Live gated)
CAR T cells
% of live cells
CD45.1+GFP+ T cells per 0.2g
c
MigR
Meso-CAR T
FAP-CAR T
60.8%
80.1%
24.8%
GFP(CAR T)
PD-1
(Single/Live/CD45.1/GFP gated)
PD-1
% of CD45.1+GFP+ T cells
d
52.8%
42.8%
84.9%
Ki-67
(Single/Live/CD45.1/GFP gated)
Ki-67
e
16.6%
23.7%
54.1%
IFN-γ
CD8
(Single/Live/CD45.1/GFP/CD8 gated)
IFN-γ
f
FAP
% of live cells
FAP-CAR T (% in total live cells)
FAP (% in total live cells)
R2=0.75
p<0.0001
Mesothelin
g
Day 1
Day 4
Day 7
CAR T/FAP/EpCAM/DAPI
CAR T cells
CAR T cells per cm2
FAP
% positive area
EpCAM
h
KPC model
PanCK/CAR T cells/FAP/DAPI
CAR T cells
PanCK

Fig. 3

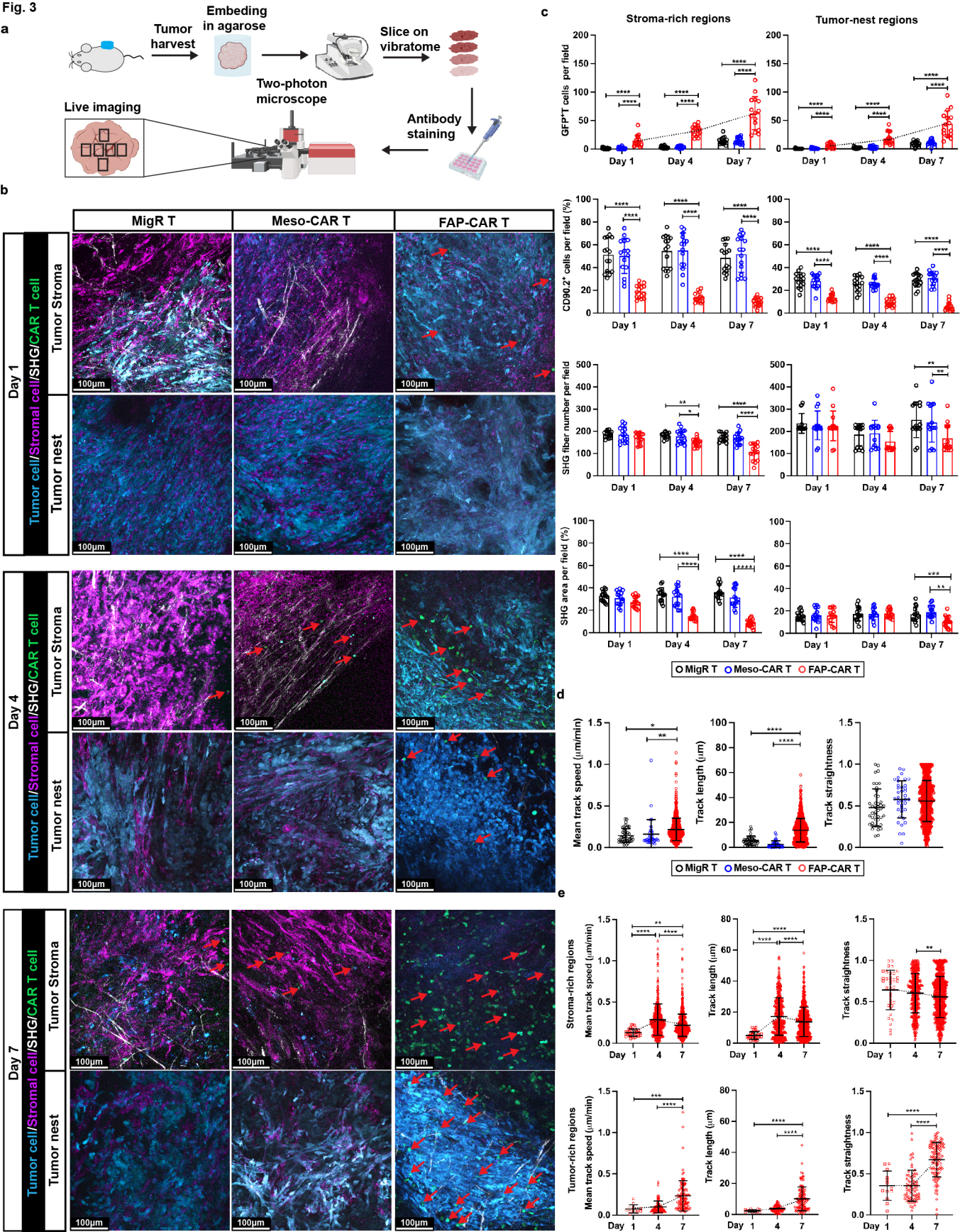
a
Tumor harvest
Embeding in agarose
Slice on vibratome
Antibody staining
Two-photon microscope
Live imaging
b
MigR T
Meso-CAR T
FAP-CAR T
Day 1
Day 4
Day 7
Tumor cell/Stromal cell/SHG/CAR T cell
Tumor Stroma
Tumor nest
100μm
c
Stroma-rich regions
Tumor-nest regions
GFP+T cells per field
CD90.2+ cells per field (%)
SHG fiber number per field
SHG area per field (%)
Day 1
Day 4
Day 7
MigR T
Meso-CAR T
FAP-CAR T
d
Mean track speed (μm/min)
Track length (μm)
Track straightness
e
Stroma-rich regions
Tumor-rich regions
Mean track speed (μm/min)
Track length (μm)
Track straightness
Day 1
4
7

Fig. 4

a

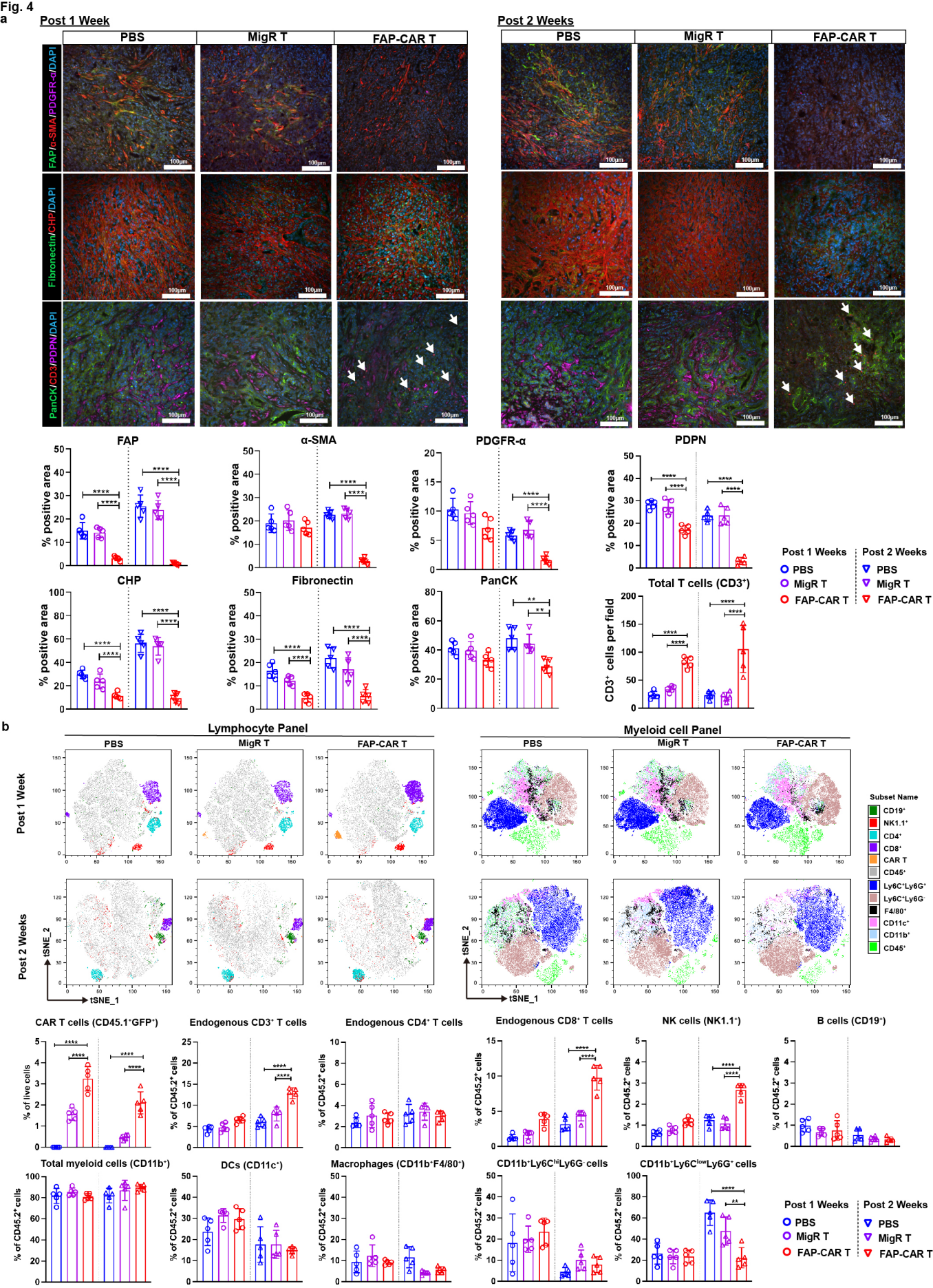
Post 1 Week
Post 2 Weeks
PBS
MigR T
FAP-CAR T
FAP/α-SMA/PDGFR-α/DAPI
Fibronectin/CHP/DAPI
PanCK/CD3/PDPN/DAPI
100μm
FAP
α-SMA
PDGFR-α
PDPN
CHP
Fibronectin
PanCK
Total T cells (CD3⁺)
% positive area
CD3⁺ cells per field
Post 1 Weeks
Post 2 Weeks
PBS
MigR T
FAP-CAR T
b
Lymphocyte Panel
Myeloid cell Panel
Post 1 Week
Post 2 Weeks
tSNE_1
tSNE_2
Subset Name
CD19⁺
NK1.1⁺
CD4⁺
CD8⁺
CAR T
CD45⁺
Ly6C⁺Ly6G⁺
Ly6C⁺Ly6G⁻
F4/80⁺
CD11c⁺
CD11b⁺
CD45⁺
CAR T cells (CD45.1⁺GFP⁺)
Endogenous CD3⁺ T cells
Endogenous CD4⁺ T cells
Endogenous CD8⁺ T cells
NK cells (NK1.1⁺)
B cells (CD19⁺)
Total myeloid cells (CD11b⁺)
DCs (CD11c⁺)
Macrophages (CD11b⁺F4/80⁺)
CD11b⁺Ly6C^hiLy6G⁻ cells
CD11b⁺Ly6C^lowLy6G⁺ cells
% of live cells
% of CD45.2⁺ cells

Fig. 5

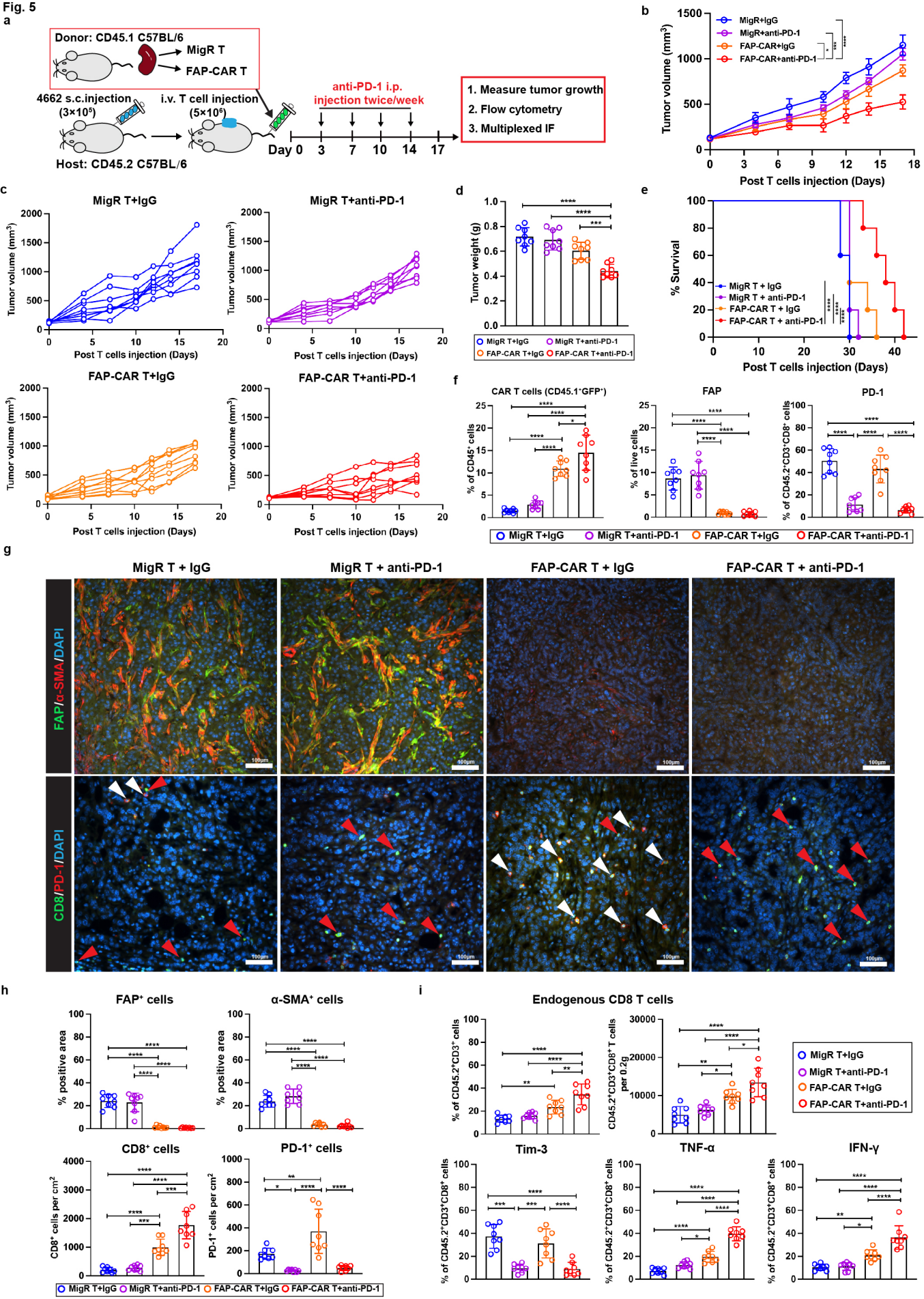
a
Donor: CD45.1 C57BL/6
MigR T
FAP-CAR T
4662 s.c.injection (3×10^5)
i.v. T cell injection (5×10^6)
Host: CD45.2 C57BL/6
anti-PD-1 i.p. injection twice/week
Day 0 3 7 10 14 17
1. Measure tumor growth
2. Flow cytometry
3. Multiplexed IF
b
Tumor volume (mm³)
Post T cells injection (Days)
MigR+IgG
MigR+anti-PD-1
FAP-CAR+IgG
FAP-CAR+anti-PD-1
c
MigR T+IgG
MigR T+anti-PD-1
FAP-CAR T+IgG
FAP-CAR T+anti-PD-1
Tumor volume (mm³)
Post T cells injection (Days)
d
Tumor weight (g)
MigR T+IgG
MigR T+anti-PD-1
FAP-CAR T+IgG
FAP-CAR T+anti-PD-1
e
% Survival
Post T cells injection (Days)
MigR T + IgG
MigR T + anti-PD-1
FAP-CAR T + IgG
FAP-CAR T + anti-PD-1
f
CAR T cells (CD45.1⁺GFP⁺)
FAP
PD-1
% of CD45⁺ cells
% of live cells
% of CD45.2⁺CD3⁺CD8⁺ cells
MigR T+IgG
MigR T+anti-PD-1
FAP-CAR T+IgG
FAP-CAR T+anti-PD-1
g
MigR T + IgG
MigR T + anti-PD-1
FAP-CAR T + IgG
FAP-CAR T + anti-PD-1
FAP/α-SMA/DAPI
CD8/PD-1/DAPI
100μm
h
FAP⁺ cells
α-SMA⁺ cells
CD8⁺ cells
PD-1⁺ cells
% positive area
CD8⁺ cells per cm²
PD-1⁺ cells per cm²
MigR T+IgG
MigR T+anti-PD-1
FAP-CAR T+IgG
FAP-CAR T+anti-PD-1
i
Endogenous CD8 T cells
% of CD45.2⁺CD3⁺ cells
CD45.2⁺CD3⁺CD8⁺ T cells per 0.2g
Tim-3
TNF-α
IFN-γ
% of CD45.2⁺CD3⁺CD8⁺ cells
MigR T+IgG
MigR T+anti-PD-1
FAP-CAR T+IgG
FAP-CAR T+anti-PD-1

Fig. 6

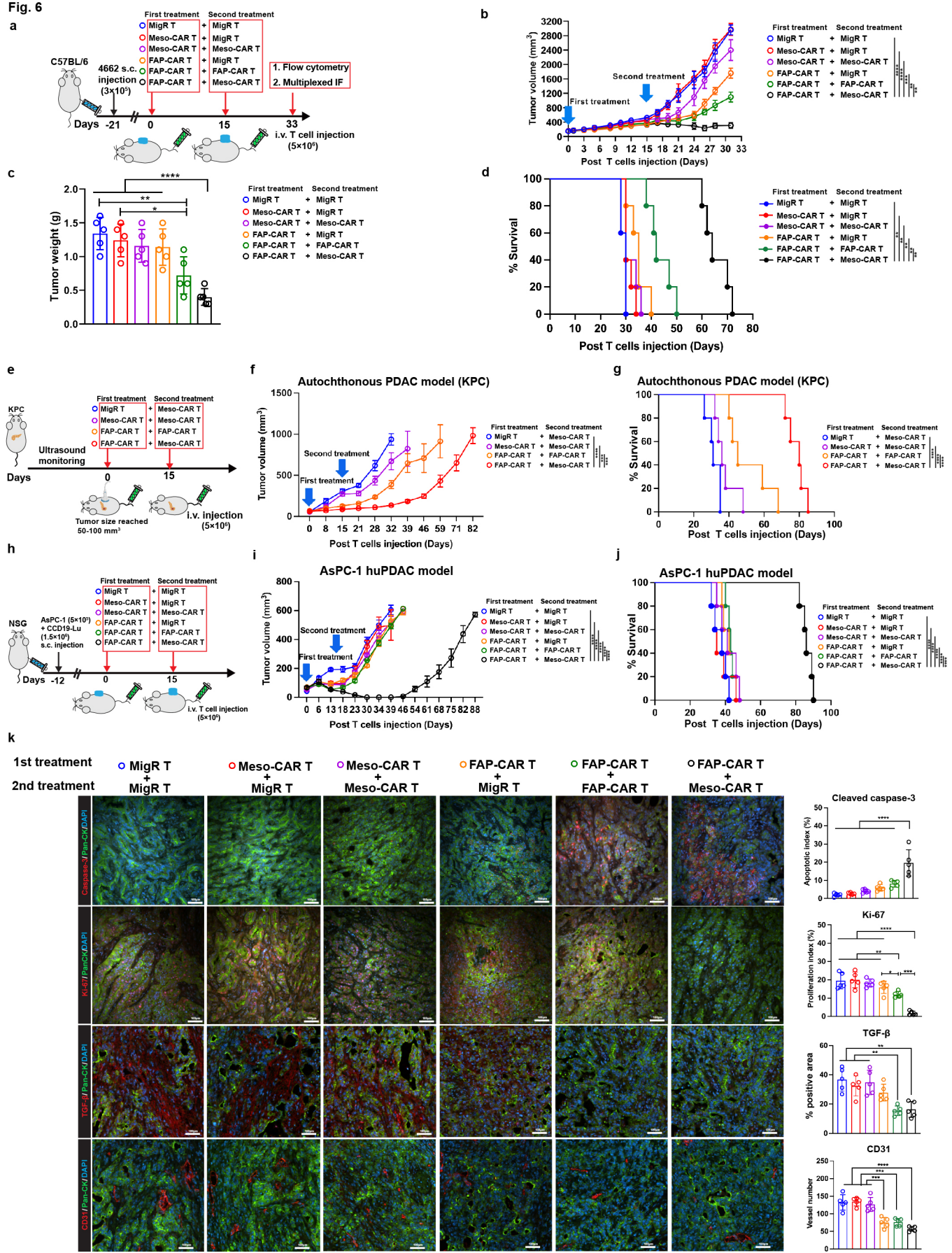
a
First treatment
Second treatment
MigR T + MigR T
Meso-CAR T + MigR T
Meso-CAR T + Meso-CAR T
FAP-CAR T + MigR T
FAP-CAR T + FAP-CAR T
FAP-CAR T + Meso-CAR T
C57BL/6
4662 s.c. injection (3×10^5)
1. Flow cytometry
2. Multiplexed IF
Days -21 0 15 33
i.v. T cell injection (5×10^6)
b
Tumor volume (mm^3)
Second treatment
First treatment
Post T cells injection (Days)
c
Tumor weight (g)
****
**
*
d
% Survival
Post T cells injection (Days)
e
KPC
Ultrasound monitoring
Days 0 15
Tumor size reached 50-100 mm^3
i.v. injection (5×10^6)
f
Autochthonous PDAC model (KPC)
Tumor volume (mm^3)
Second treatment
First treatment
Post T cells injection (Days)
g
Autochthonous PDAC model (KPC)
% Survival
Post T cells injection (Days)
h
NSG
AsPC-1 (5×10^6) + CCD19-Lu (1.5×10^6) s.c. injection
Days -12 0 15
i.v. T cell injection (5×10^6)
i
AsPC-1 huPDAC model
Tumor volume (mm^3)
Second treatment
First treatment
Post T cells injection (Days)
j
AsPC-1 huPDAC model
% Survival
Post T cells injection (Days)
k
1st treatment
2nd treatment
MigR T + MigR T
Meso-CAR T + MigR T
Meso-CAR T + Meso-CAR T
FAP-CAR T + MigR T
FAP-CAR T + FAP-CAR T
FAP-CAR T + Meso-CAR T
Caspase-3/Pan-CK/DAPI
Ki-67/PanCK/DAPI
TGF-β/Pan-CK/DAPI
CD31/Pan-CK/DAPI
Cleaved caspase-3
Apoptotic index (%)
Ki-67
Proliferation index (%)
TGF-β
% positive area
CD31
Vessel number

Fig. 7

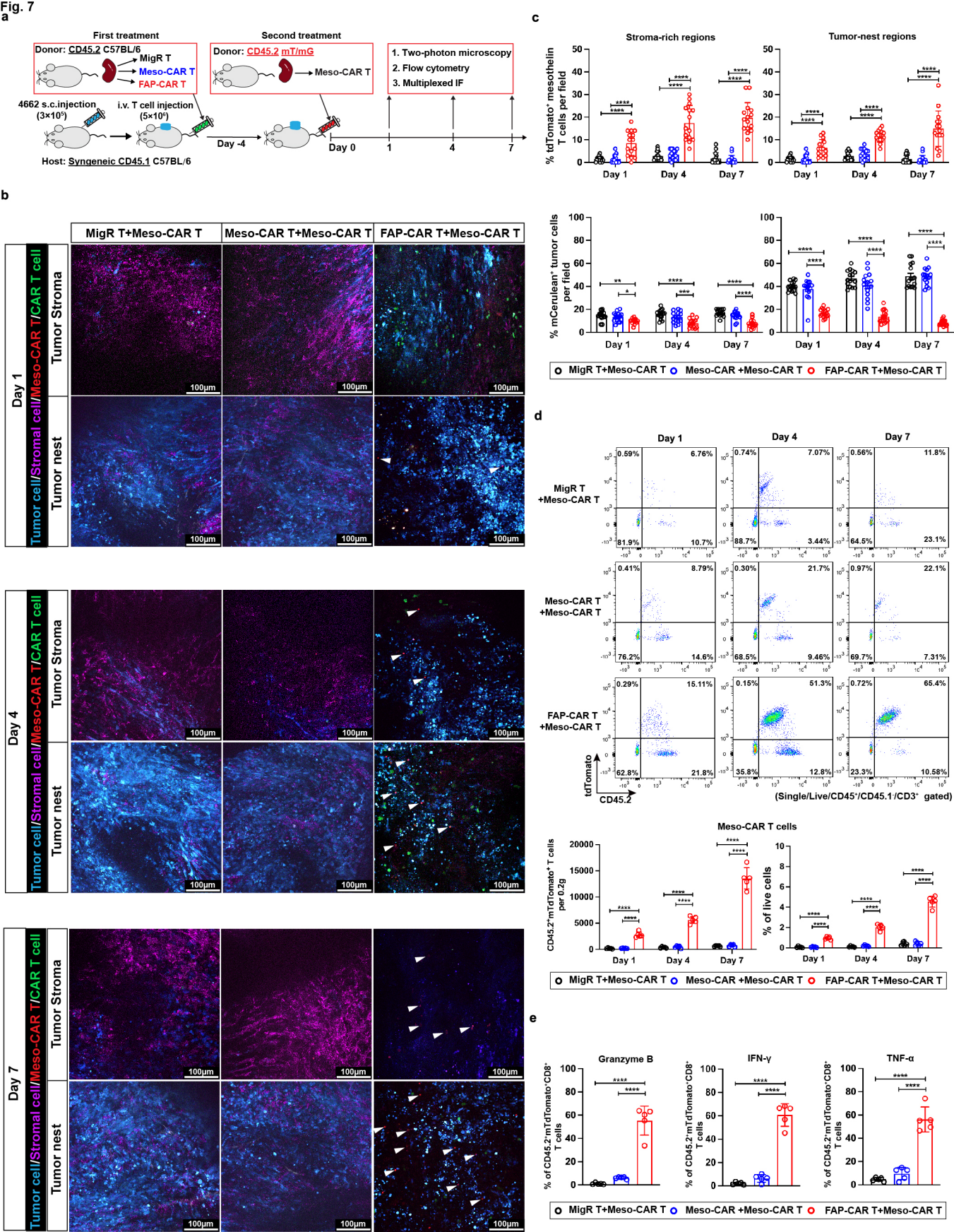
a
First treatment
Donor: CD45.2 C57BL/6
MigR T
Meso-CAR T
FAP-CAR T
Second treatment
Donor: CD45.2 mT/mG
Meso-CAR T
1. Two-photon microscopy
2. Flow cytometry
3. Multiplexed IF
4662 s.c.injection (3×10^5)
i.v. T cell injection (5×10^6)
Day -4
Day 0
1
4
7
Host: Syngeneic CD45.1 C57BL/6
b
MigR T+Meso-CAR T
Meso-CAR T+Meso-CAR T
FAP-CAR T+Meso-CAR T
Day 1
Day 4
Day 7
Tumor Stroma
Tumor nest
Tumor cell/Stromal cell/Meso-CAR T/CAR T cell
100μm
c
Stroma-rich regions
Tumor-nest regions
% tdTomato+ mesothelin T cells per field
% mCerulean+ tumor cells per field
Day 1
Day 4
Day 7
MigR T+Meso-CAR T
Meso-CAR +Meso-CAR T
FAP-CAR T+Meso-CAR T
d
MigR T +Meso-CAR T
Meso-CAR T +Meso-CAR T
FAP-CAR T +Meso-CAR T
tdTomato
CD45.2
(Single/Live/CD45+/CD45.1-/CD3+ gated)
Meso-CAR T cells
CD45.2+mTdTomato+ T cells per 0.2g
% of live cells
e
Granzyme B
IFN-γ
TNF-α
% of CD45.2+mTdTomato+CD8+ T cells

Fig. 8

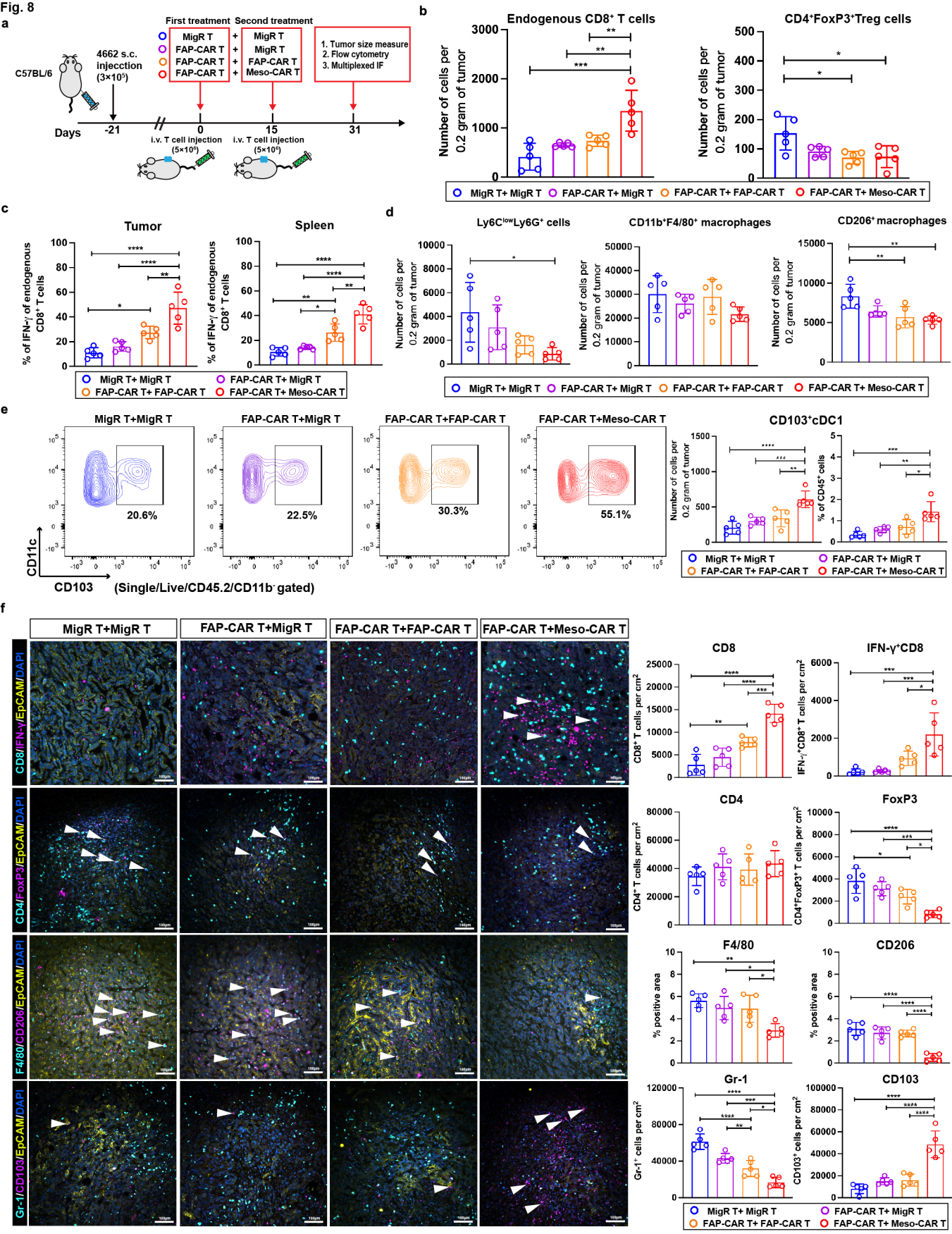
a
First treatment
Second treatment
MigR T
FAP-CAR T
FAP-CAR T
FAP-CAR T
+
MigR T
MigR T
FAP-CAR T
Meso-CAR T
1. Tumor size measure
2. Flow cytometry
3. Multiplexed IF
C57BL/6
4662 s.c. injecction (3×10^5)
Days
-21
0
15
31
i.v. T cell injection (5×10^6)
i.v. T cell injection (5×10^6)
b
Endogenous CD8+ T cells
CD4+FoxP3+Treg cells
Number of cells per 0.2 gram of tumor
MigR T+ MigR T
FAP-CAR T+ MigR T
FAP-CAR T+ FAP-CAR T
FAP-CAR T+ Meso-CAR T
c
Tumor
Spleen
% of IFN-γ of endogenous CD8+ T cells
d
Ly6ClowLy6G+ cells
CD11b+F4/80+ macrophages
CD206+ macrophages
e
MigR T+MigR T
FAP-CAR T+MigR T
FAP-CAR T+FAP-CAR T
FAP-CAR T+Meso-CAR T
20.6%
22.5%
30.3%
55.1%
CD103+cDC1
% of CD45+ cells
CD11c
CD103
(Single/Live/CD45.2/CD11b- gated)
f
CD8/IFN-γ/EpCAM/DAPI
CD4/FoxP3/EpCAM/DAPI
F4/80/CD206/EpCAM/DAPI
Gr-1/CD103/EpCAM/DAPI
CD8
IFN-γ+CD8
CD4
FoxP3
F4/80
CD206
Gr-1
CD103
CD8+ T cells per cm2
IFN-γ+CD8+ T cells per cm2
CD4+ T cells per cm2
CD4+FoxP3+ T cells per cm2
% positive area
Gr-1+ cells per cm2
CD103+ cells per cm2